LIDAR-BASED FRACTURE CHARACTERIZATION: AN OUTCROP-SCALE STUDY OF THE WOODFORD SHALE, MCALISTER SHALE PIT, OKLAHOMA

By

JASON HANZEL

Bachelor of Science

Oklahoma State University

Stillwater

2012

Submitted to the Faculty of the
Graduate College of the
Oklahoma State University
in partial fulfillment of
the requirements for
the Degree of
MASTER OF SCIENCE
July, 2014

LIDAR-BASED FRACTURE CHARACTERIZATION:

AN OUTCROP-SCALE STUDY OF THE WOODFORD

SHALE, MCALISTER SHALE PIT, OKLAHOMA

Thesis Approved:

Dr. Priyank Jaiswal

Thesis Adviser

Dr. Jeffrey M. Byrnes

Dr. Jim Puckette

Dr. Mohamed Abdel Salam

ACKNOWLEDGEMENTS

I would like to thank Oklahoma State University, the Boone Pickens School of Geology, American Association of Petroleum Geologists-Oklahoma State University Geoscience GIS Consortium, the Geology Student Enrichment Fund, Oklahoma State University Core Facility for Laser-Based Three-Dimensional Scanning and Chesapeake Energy for providing me with financial support during my graduate studies. In addition, I would like to thank my adviser Dr. Priyank Jaiswal, and my committee members Dr. Jeffrey M. Byrnes, Dr. Jim Puckette and Dr. Mohamed Abdel Salam for their knowledge and guidance. I give my sincere thanks to Tan Nguyen at *RIEGL USA* for all his assistance and help with RiSCAN PRO throughout my project. I want to thank Brian Gary and Brian Norton for their help with the Split-Fx software. I also wish to acknowledge my future employer, Concho Resources, who gave me an amazing opportunity as an intern the summer of 2013. Since my internship to the present, Concho has been supportive and provided much encouragement. I am particularly grateful for the assistance in the field by Logan Chatterton, Malachi Lopez, Dr. Daniel Lao Davila, Curtis Roddy and friendships given by my fellow graduate students. Lastly, I would like to acknowledge Megan and my family. This would not have been possible without their constant encouragement and support.

Name: JASON HANZEL

Date of Degree: JULY, 2014

Title of Study: LIDAR-BASED FRACTURE CHARACTERIZATION: AN OUTCROP-SCALE STUDY OF THE WOODFORD SHALE, MCALISTER SHALE PIT, OKLAHOMA

Major Field: GEOLOGY

Abstract:

The use of lidar (light detection and ranging), a remote sensing tool based on principles of laser optometry, in mapping complex, multi-scale fracture networks had not been rigorously tested prior to this study despite its foreseeable utility in interpreting rock fabric with imprints of complex tectonic evolution. This thesis demonstrates lidar-based characterization of the Woodford Shale where intense fracturing could be due to both tectonism and mineralogy. The study area is the McAlister Shale Pit in south-central Oklahoma where both the upper and middle sections of the Woodford Shale are exposed and can be lidar-mapped. Lidar results are validated using hand-measured strike and dips of fracture planes, thin sections and mineral chemistry of selected samples using X-ray diffraction (XRD). Complexity of the fracture patterns as well as inaccessibility of multiple locations within the shale pit makes hand-measurement prone to errors and biases; lidar provides an opportunity for less biased and more efficient field mapping.

Fracture mapping with lidar is a multi-step process. The lidar data are converted from point clouds into a mesh through triangulation. User-defined parameters such as size and orientation of the individual triangular elements are then used to group similar elements into surfaces. The strike and dip attribute of the simulated surfaces are visualized in an equal area lower hemisphere projection stereonet. Three fracture sets were identified in the upper and middle sections with common orientation but substantially different spatial density. Measured surface attributes and spatial density relations from lidar were validated using their hand-measured counterparts.

Thin section analysis suggests that high fracture density in the upper Woodford measured by both the lidar and the hand-measured data could be due to high quartz. A significant finding of this study is the reciprocal relation between lidar intensity and gamma-ray (GR), which is generally used to infer outcrop mineralogy. XRD analysis of representative samples along the common profiles show that both GR and lidar intensity were influenced by the same minerals in essentially opposite ways. Results strongly suggest that the lidar cannot only remotely map the geomorphology, but also the relative mineralogical variations to the first order of approximation.

TABLE OF CONTENTS

Chapter Page

LIST OF TABLES

Table Page

LIST OF FIGURES

Figure Page

CHAPTER I

INTRODUCTION

1.1 Problem

Within the last decade, horizontal drilling and hydraulic fracturing technology has allowed source rocks, such as the Devonian-Mississippian Woodford Shale, to be used as reservoirs. Fracability, i.e., the likelihood of complex fracture networks being created in the rock when it is stimulated by pumped fracturing fluids, is a decisive factor that governs the production of oil and gas from plays like Woodford Shale. Fracability can be potentially related to pre-existing planes of weakness in the rock, such as joints and fractures, which could ultimately be a manifestation of the paleo-stress regime in the rock fabric (Pollard and Aydin, 1988; Fritz et al., 1991; Maher, 2007; Ataman, 2008; Varacchi, 2011). For the purposes of this thesis fractures and joints are defined as discontinuities in the rock fabric that arise from mechanical rupture (Laderia, 1981; Candela et al., 1997). Although fracturing is a result of mechanical processes, the extent that fracturing is affected (and ultimately shaped) by chemical/mineralogical differences in rock composition is not well understood. Mineralogical constituents such as dolomite and quartz are known to increase brittleness in a rock, creating higher fracture densities (Brace, 1961; Hobbs, 1967; Nelson, 1985; Corbett et al., 1987; Narr and Suppe, 1991; Gross et al., 1995; Hatcher, 1995; Henning et al., 2000; Underwood et al., 2003; Ataman, 2008; Laubach et al., 2009; Cardott, 2012; Romero and Philp, 2012). However, the dependence of fracture patterns on mineralogy remains scarcely investigated for the Woodford Shale.

1.2 Lidar

This thesis exclusively uses a terrestrial lidar (light detection and ranging) scanner. Such lidar technology is a remote sensing approach that measures distances by emitting laser to illuminate a target and analyzing the reflected pulse. The main components of a lidar system include electronics to emit laser pulses and then to record the returning reflections. The narrow aperture of the laser beam allows mapping of physical features at millimeter-scale resolution. The narrow aperture of the laser beam allows mapping of physical features at millimeter-scale high resolution. In general, ultraviolet, visible and near infrared wavelengths lasers can be used for lidar mapping.

Lidar scanners can map centimeter- to millimeter-scale relief. A significant advantage of acquiring lidar data is that they can be appropriately preconditioned to automate delineation of bedding and fractures surfaces, measurements of strike and dip (Rotevatn et al., 2009; Portas and Slatt, 2010; Burton et al., 2011) and characteristics of discontinuities in terms of their orientation, and spacing (Feng and Roeshoff, 2004). Due to its accuracy and efficiency in areal coverage, lidar has been successfully applied in several geological studies such as in mapping slopes (Kemeny and Donovan, 2005; Sturzenegger et al., 2007; Inada and Takagi, 2010), monitoring land management (Ehinger, 2010; Bond, 2011), characterizing surface roughness (Candela et al., 2009), inferring stratigraphy (Bellian et al., 2005; Nagihara, 2006), coastal mapping (Wozencraft and Millar, 2005) and outcrop characterization (Feng and Roeshoff, 2004; Rotevatn et al., 2009; Moore et al., 2012). Lidar data have two attributes – spatial and spectral. Researchers tend to focus on either. The spatial aspect, which is the high-resolution morphological character of a reflector, makes lidar a popular tool for mapping stratigraphic and geometrical relationships (Feng and Roeshoff, 2004; Monte, 2004; Nagihara, 2006; Sturzenegger et al., 2007; Inada and Takagi, 2010; Ehinger, 2010; Bond, 2011). Much like the peer studies referenced above, the spatial attribute was primarily used in this study for fracture detection. Fracture (orientation

and/or density) is not an automated process of lidar. The point-cloud dataset, which is a collection of individual reflectors from the outcrop face in 3D, needs to be processed to automate identification of different geomorphological features such as drainage or fractures. Besides spatial data, lidar instruments can also record intensity, which is the power of the backscattered signal relative to the power of the emitted signal and can potentially discriminate mineralogy (Burton et al., 2011).

This application uses a *RIEGL* VZ-400 scanner which is a full-waveform lidar scanner using near-infrared pulses. The scanner was provided by the Core Facility for Laser-Based Three-Dimensional Scanning at Oklahoma State University. Based on the dimensions, distance and orientation of the target, a single laser pulse can generate multiple returns. Rotating mirrors in VZ-400 provide fully linear, unidirectional and parallel pulses. The online waveform processing allows reflected information to be attained at a high rate (thousands of points per second). The distance of a reflector is then calculated by the formula (Kemeny and Donovan, 2005; Ehinger, 2010; Bond, 2011): Distance = (Speed of Light * Time of Flight)/2, where "Time of Flight" is time it takes for the optical pulse to travel to a reflected surface and back. VZ-400 emits another pulse slightly horizontal and vertical to the previous one in a continuous fashion (Bellian et al., 2005).

1.3 Significance

Up to 8% of the world's original hydrocarbon reserves are estimated to have been sourced by the Woodford Shale (Fritz et al., 1991). In the primary oil-producing region of central and southern Oklahoma, 22 billion barrels of bitumen and 16 billion barrels of saturated hydrocarbons are estimated to have been expelled from Woodford Shale (Comer, 1987). As the Woodford Shale matured, its internal fractures served as migration pathways for hydrocarbon to escape into nearby formations. However, it is suggested that due to a micropore system that not

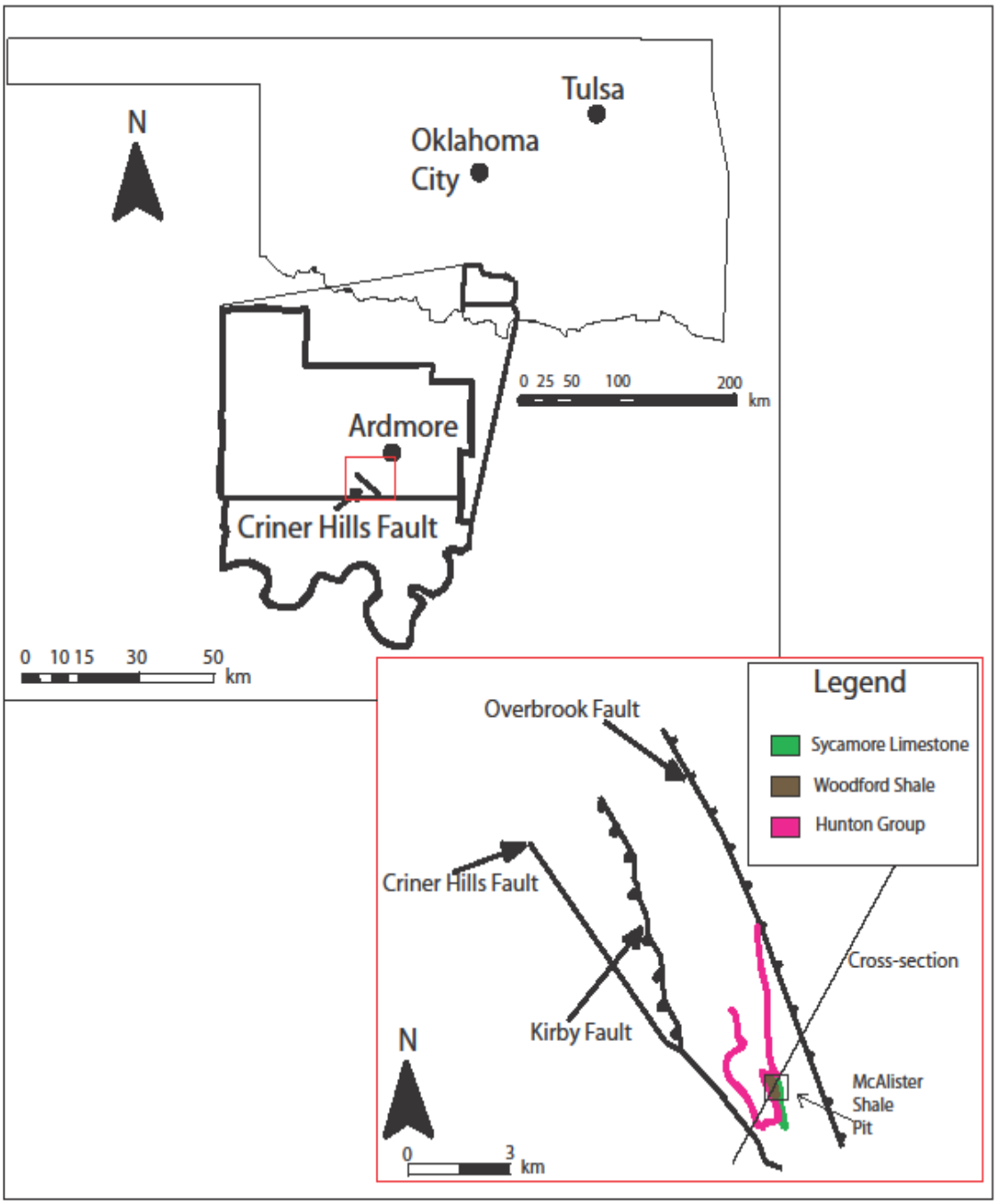

Figure 1 – Map showing the location of McAlister Shale Pit outcrop in southern Oklahoma (modified from Walker, 2006). The inset geological map shows outcrop patterns for the lithostratigraphic units present in the project area. A cross section line from Figure 2 is depicted in the inset map.

all hydrocarbons migrated out of the Woodford Shale (Comer, 1987). Bitumen occurs in joints and small-scale fractures in the Woodford Shale at the outcrop level (Bernal et al., 2012). Thus, studying natural fracture patterns in the Woodford Shale serves as an important tool in understanding fracture spacing and geometry.

The study area in this thesis is the McAlister Shale Pit pivots on three distinct advantages over field mapping by hand. First, the intensely fractured fabric of the Woodford Shale has multi-dimensional and multi-orientation fractures (Guo et al., 2010), all of which cannot be effectively mapped by hand in an unbiased manner. In principle, however, the outcrop surface can be captured within a lidar scan in adequately high resolution to allow computer-guided, potentially unbiased mapping. Second, zones that are physically inaccessible can also be accessed through a lidar scan. Third, the lidar data not only replicates the surface roughness in 3D but also the intensity of reflection from discrete locations. This provides the opportunity to analyze the fracture density and orientation in context of the weathering pattern for the outcrop surface and potentially relate them to other rock properties such as the mineralogy. The lidar data in this thesis is augmented by field-gathered strike and dip measurements taken using a Brunton© transit, linear fracture density measurement along random profiles (hereafter referred to as scanlines), and rock samples for x-ray diffraction (XRD) along the scanline.

CHAPTER II

BACKGROUND

2.1 Woodford Shale

The Woodford Shale, which extends from present day Kansas into Texas, is recognized as a premier quality source rock that charged most oil-producing fields in the Mid-Continent (Comer and Hinch, 1987). A distinctive characteristic of the Woodford Shale sections on well logs is higher radioactivity as recorded by the gamma-ray (GR) curve, which shows the shale as radioactive compared to superjacent and underlying carbonates (Lewan, 1983). Contrary to conventional understanding, Blackford (2007) showed that gamma-ray values for the Woodford Shale may not always correspond positively with higher total organic carbon (TOC), a finding that supports the premise that the Woodford Shale mineralogy can be quite variable. Studies such as Cardott and Lambert (1985), Sullivan (1985), Hester (1990), Kirkland et al. (1992), Lambert (1993), Comer (2005), Harris et al. (2009), Neman (2011), Romero and Philp (2012), and Cardott (2012) demonstrated that the anoxic or euxenic conditions that help preserve carbon and generate source rocks were not temporally or spatially continuous during deposition of Woodford Shale sediments. Climatic and eustatic variations resulted in at least three, typically compositionally distinct, informal sections referred to as the upper, middle and the lower sections.

The lower section, Devonian-Frasian/Famennian in age, is a near-shore transgressive facies. It has the highest clay concentration and the smallest areal extent (Portas and Slatt, 2010). The middle section is more distal than the lower section. Slow deposition rate resulted in

diffusions of uranium, high-Mg dolomite, the highest TOC values and concentration of heavy minerals, such as pyrite, and the greatest areal extent (Blackford, 2007). The upper section of the Woodford Shale, Devonian-Famennian to early Mississippian-Tournaisian in age, is the most proximal facies and contains the highest chert concentration due to upwelling conditions (Puckette et al, 2013). The upper section has the lowest TOC and abundant phosphate (in the form of nodules). The silica in the upper section is directly related to the abundance of radiolarians. As subsistence of induced fractures requires a brittle rock matrix, from a resource development perspective, high quartz content in the middle section makes it lucrative target (Cardott and Lambert, 1985; Hester et al., 1990; Harris et al., 2009; Badra, 2011; Bernal et al., 2012). However, brittleness is not the only criteria for productivity, TOC and cementation can also play a vital role (Blackford, 2007).

Marfurt and Kirlin (2000) showed how deformation can induce joints and fractures in clay. They also observed that the fracture density and magnitude changed from one material to another, implying that fracture patterns and rheology may be related (Narr and Suppe, 1991; Gross et al., 1995; Hennings et al., 2000). In the case of the Woodford Shale, the prevalence of natural fractures has been well documented (Cardott 1985; Hester 1990; Comer 2005; Ataman 2008; Harris 2009). Using seismic data, Guo et al. (2010) show that fractures in Woodford Shale are multidirectional. Understanding the natural fracture patterns in terms of their orientation, density, and evolution can be critical to resource development (Gross et al., 1995; Laubach et al., 2009).

2.2 McAlister Shale Pit

The McAlister Shale Pit is located in southern Oklahoma eight miles south of Ardmore, Oklahoma (NE 1/4 SW1/4, Sec.36, T.5S, R1E), on the Overbrook Anticline northeast of the Criner Hills and Criner fault (Walker 2006; Figure 1). The Overbrook Anticline, which trends

NW-SE and formed during the Pennsylvanian, is a topographic high west of the Ardmore Basin (Walker, 2006). The Criner Hills are an intensely folded and faulted region (Walker, 2006; Ataman, 2008; Badra, 2011). Figure 2, depicts a modified paleo-cross section of southern Oklahoma, (Allen, 2002) highlighting the Criner Hills deformation and exposure of the Woodford Shale seen in the McAlister Shale Pit. A stratigraphic column for southern Oklahoma is provided in Figure 3.

Organic matter in the Woodford Shale in the Ardmore basin is dominated by type II kerogen (Romero and Philp, 2012). Although the Ardmore basin has other Woodford Shale outcrops, the advantage of McAlister Shale Pit is the presence of all three sections (Badra, 2011; Bernal et al., 2012; Puckette et al., 2013; Figure 4). For the purposes of this thesis, data (lidar and hand-sampled) from the upper and middle sections are considered adequate. Due to a sizeable exposure of all three sections, the McAlister Shale Pit has been a site of several generations of studies ranging from basic fracture mapping to advanced organic geochemistry. In the shale pit, the Woodford Shale is fissile toward the base (lower section) and beds thicken to more siliceous shale at the top (upper section). Even with in the upper section, the Woodford Shale is more fissile between siliceous beds with phosphate nodules. In all three sections, bedding planes strike generally NW-SE and dip NE. Due to geometry of fractures the lower section was not exposed effectively enough to show robust fracture results. Thus to provide the best conclusions for the region, lidar mapping was conducted in the upper and the middle sections due exposure and relief (~10 m and ~4 m respectively), which allowed bedding perpendicular views.

Previously at this site, Ataman (2008) noted the presence of two dominant fracture sets, both striking NE (perpendicular to bedding) and dipping NW and SE, respectively, and suggested that the two sets were conjugate. Ataman (2008) also reported the presence of a less prevalent set parallel to the strike of the bedding planes and concluded that while the conjugate set was formed

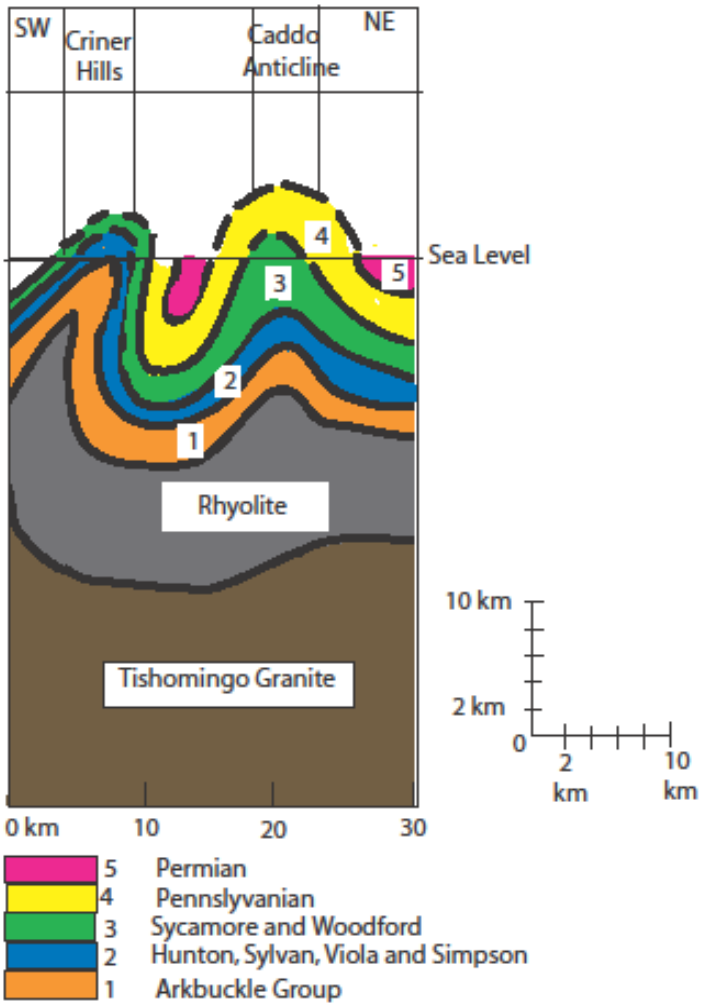

Figure 2 – Modified generalized paleo-cross section from Allen (2002) depicting the Criner Hills Uplift to Caddo Anticline after the Arbuckle Orogeny. Cross section line can be seen in Figure 1.

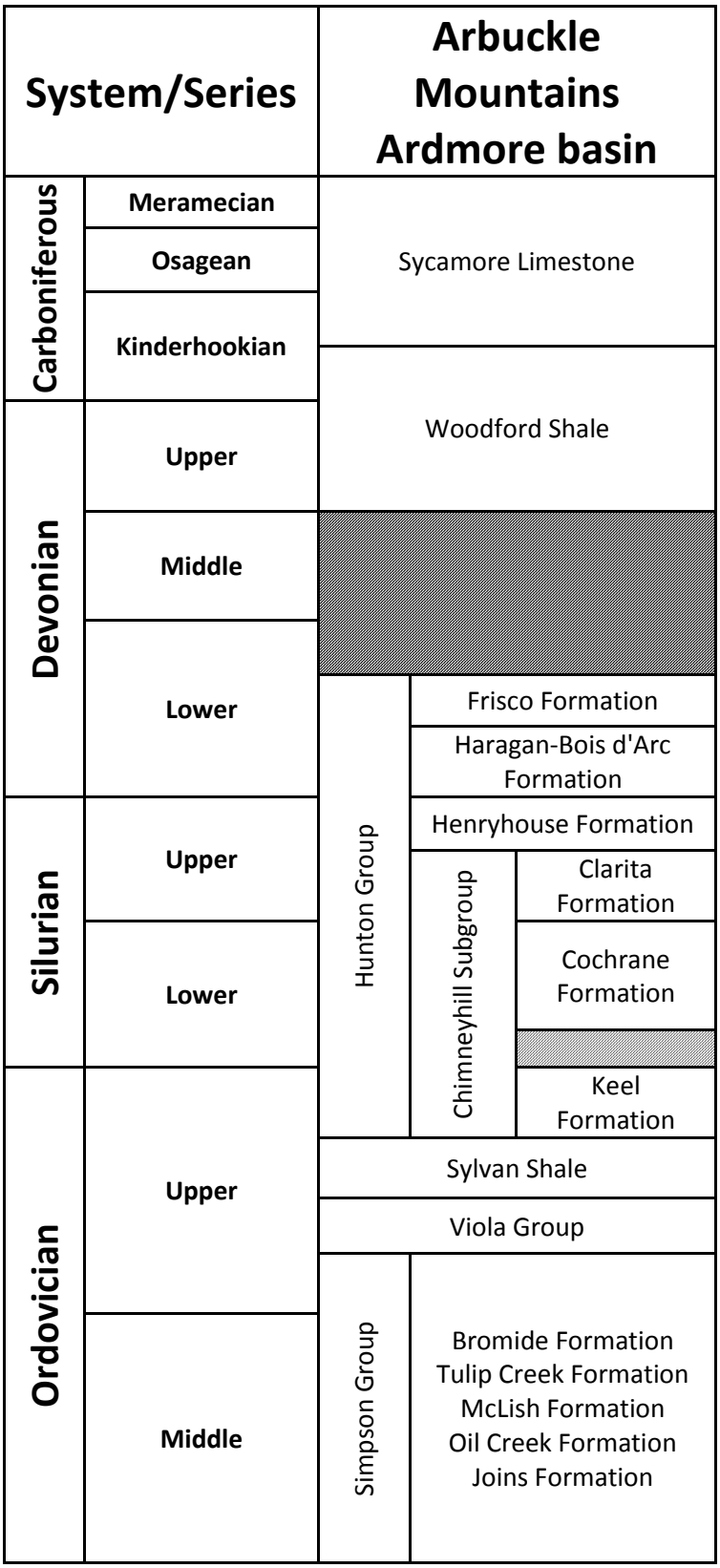

Figure 3 - Stratigraphic nomenclature for the Ordovician through Mississippian section in the Arbuckle Mountains and Ardmore Basin, south-central Oklahoma (Blackford, 2007; Ataman, 2008; Portas and Slatt, 2010).

during regional stresses prior to or during the evolution of the Arbuckle Anticline, the less prevalent set could be younger in age.

Sequence stratigraphy at the McAlister Shale was recently proposed by Bernal et al. (2012), who analyzed organic carbon in conjunction with gamma ray and identified transgressive and highstand systems tracts. This work not only confirmed the extent of the three sections, but also confirmed that the region has type II kerogen with TOC varying from 4-12%, with vitrinite reflectance (Ro) ~0.43 suggesting bitumen and degraded vitrinite. Type II kerogens arise from several very different sources, including marine algae, pollen and spores, leaf waxes, and fossil resin (Hendrick, 1990). Most type II kerogens are found in marine sediments deposited under reducing conditions (Romero and Philp, 2012). Also, XRD and scanning electron microscopy (SEM) analyses for the middle section suggest heterogeneity in the Woodford Shale as adjacent beds vary in quartz and clay content. Puckette et al. (2013) show that chert and phosphate are abundant immediately below the Devonian-Mississippian contact; this is the upper section. In these locations the presence of altered chert beds as well as phosphate rich beds reduces GR compared to the middle and the lower sections.

2.3 Initial Work

To set up the framework of this study, a lab- and field-based exercise was conducted. Thin sections from the three sections of the Woodford Shale at the McAlister Shale Pit were analyzed to visually confirm that, as suggested in the literature, the relative proportion of silica to clay increases upward from the lower to the upper sections of the Woodford Shale (Figure 5). The potential relationship between rock composition and fracture density is evident in thin sections from the lower section of the Woodford Shale (Figure 6). The first thin section (Figure 6B) is from a 5 cm thick bed, with a noticeably higher linear density of fractures. The second thin section is from a more fissile 5.5 cm thick bed with a diminutive presence of fractures compared

Figure 4 – Study area image data. (A) Google Earth image of the study area showing the landscape in the vicinity of McAlister Shale Pit. The shale pit is labeled and its extent is marked. (B) First order interpretation of the pit showing the three broad sub-sections of Woodford Shale. In the plan view, although the relative exposure of all the three sub-sections are comparable, the upper and the middle sections have more relief and are therefore better for lidar mapping.

to the previous bed. The first thin section contains 0.5 millimeter thick alternating silica-rich laminae interbedded with *Tasmanites*/organic-rich laminae (Figure 6B). The second section, which has fewer fractures, was devoid of apparent silica (Figure 6C). In this particular sample set, the presence of silica directly affects the fracture density.

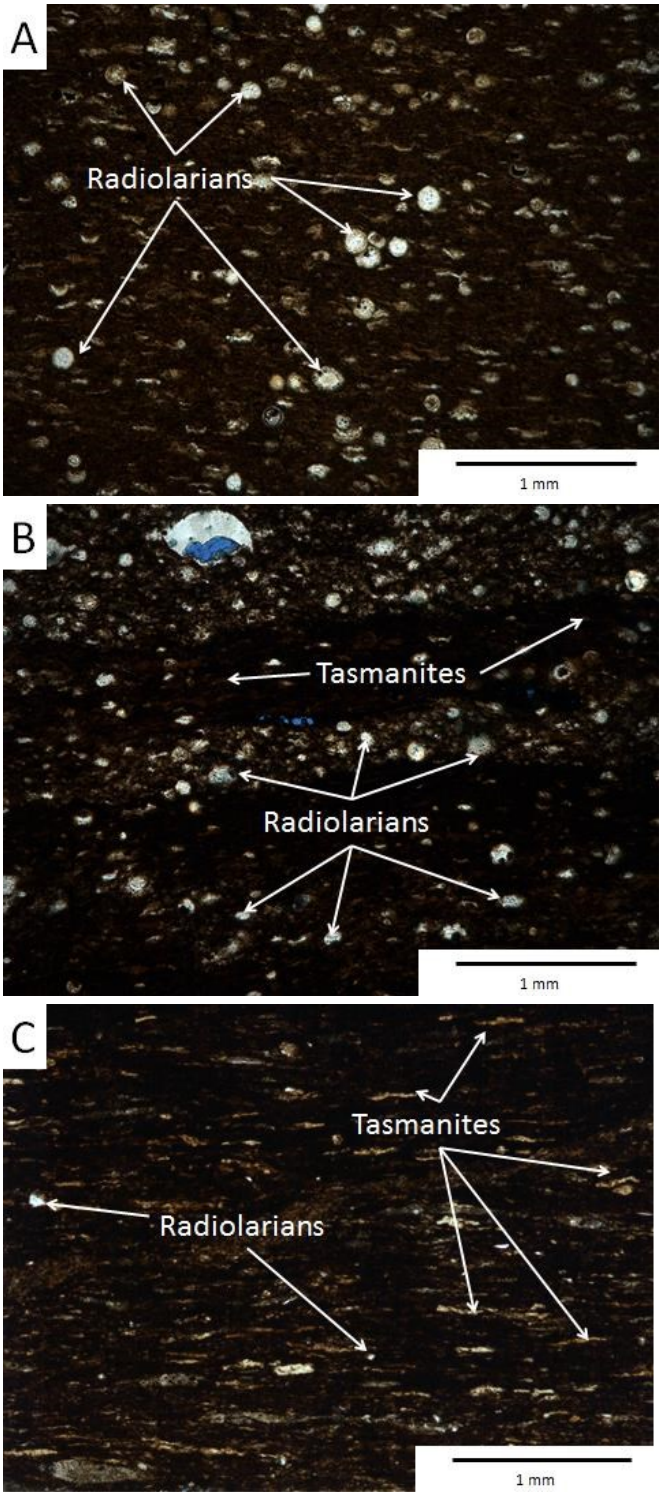

Figure 5 – Thin section photomicrographs of representative images of Woodford Shale in cross polarized light (A) upper section with abundant radiolarians, (B) middle section with radiolarian and *Tasmanite* cysts, and (C) lower section with sparse radiolarians, but relatively abundant *Tasmanite cysts*. Comparatively as a progression is made from c to a, an increase of silica can be noticed.

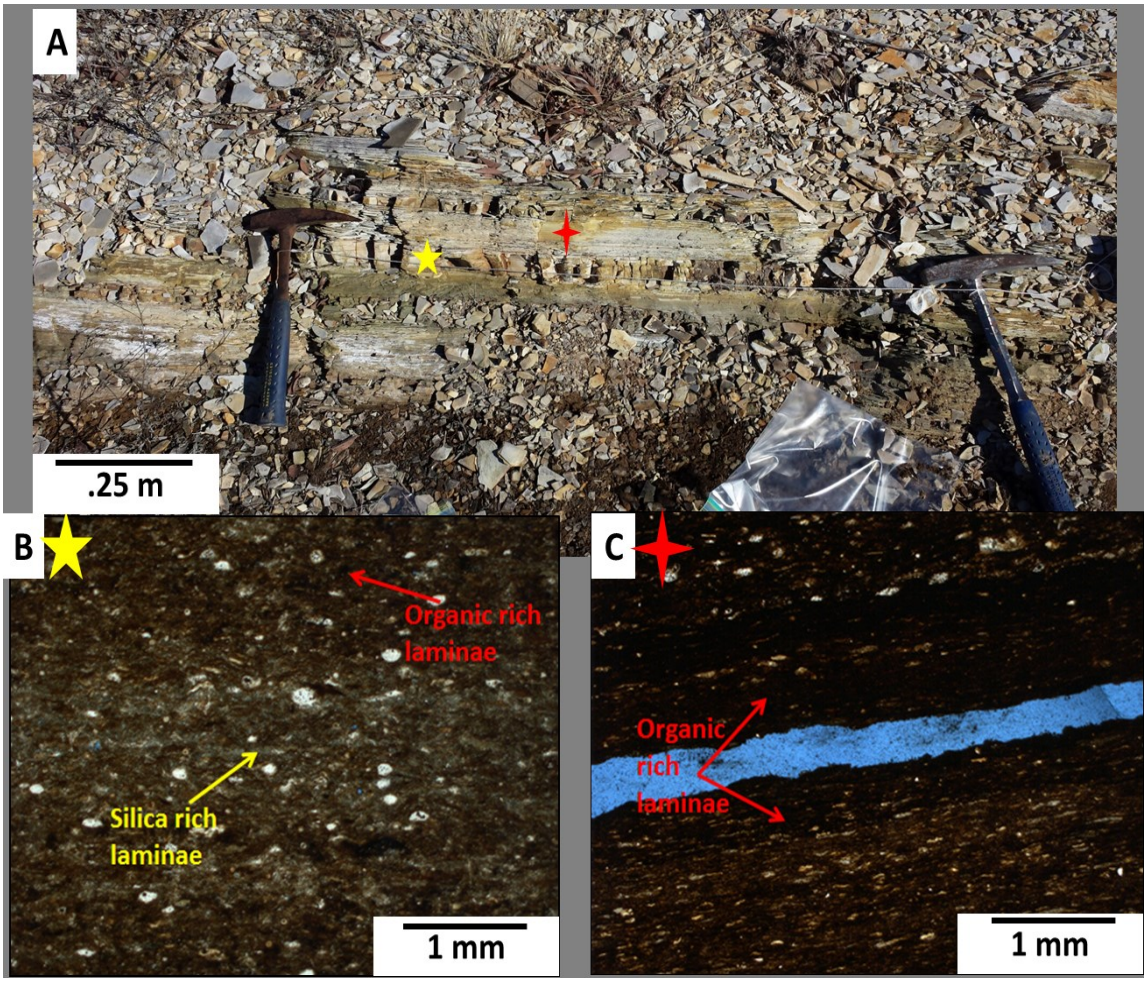

Figure 6 – Mineralogy versus rock fabric. (A) Photograph from lower section of the Woodford Shale showing heterogeneity. Yellow and red stars show sampling locations for thin sections. (B) Thin section photomicrograph from the location marked with the yellow star showing silica-rich and organic-rich laminae. (C) Thin section photomicrograph from the location marked with a red star showing absence of silica-rich laminae. These small-scale changes in mineralogy result in visible differences in texture.

CHAPTER III

METHODOLOGY

3.1 Lidar Data Acquisition

The VZ-400 scanner is a fully integrated system with emitting and receiving electronics (Figure 7). Table 1 shows performance parameters of the scanner set for this study. Besides the scanner, equipment used to complete the data acquisition included a scanner tripod, power cables, two car batteries (only one is required for short field collection session of 5-6 hours depending on scan length), camera with camera USB cable, eight carbon fiber rods with tripods, eight cylinder reflectors, and a Panasonic Toughbook laptop. Similar to traditional field work, lidar acquisition requires time spent understanding the field site to determine what needs to be imaged and the number of required scans. A general rule to follow (with the VZ-400) when determining scan position locations is that the scanner distance to the target surface needs to be at least one

	Long Range Mode	**High Speed Mode**
Pulse repetition rate PRR (peak)	100 kHz	300 kHz
Effective Measurement Rate	42,000 measurements/sec	122,000 measurements/sec
Max. Measurement Range		
natural targets ρ ≥ 90%	600 m	350 m
natural targets ρ ≥ 20%	280 m	160 m
Max. Number of Targets per Pulse	practically unlimited	
Accuracy	5 mm	
Precision	3 mm	

Table 1 – Range performance for a *RIEGL* VZ-400 scanner (http://riegl.com/uploads/tx_pxpriegldownloads/DataSheet_VZ-400_18-09-

Figure 7 – Field photograph of data acquisition with the VZ-400

half the height of the intended target. This allows for the entire rock face to be included in the scan as well as helps eliminate sharp angles between the scanner field and possible dip of the face.

Despite the best efforts, as in any geophysical acquisition, data comprises both adequately and inadequately sampled parts of the geology. As a result, shadow zones (zones of no reflectivity) appear, which pose a challenge in processing and interpretation. In this study, shadow zones are likely generated by fractures that run parallel to the direction of the lidar pulse. This configuration results in a shooting angle such that no energy is reflected back to the scanner. In principle, making multiple scans of a face from different angles can compensate for shadow zones. In this application, the shadow zone problem was mitigated by photo draping, which

allowed visual identification of the fractures. Fractures were also identified and measured by hand.

Set-up before and the individual scans are time consuming, making it even more important to take time to understand the geometries of each scan and placement of the scanner and reflectors. To better appreciate reflector placement, the quadrant rule must be understood, for each scan position a minimum of one reflector should be placed in a position to be visible in each of the four quadrants. This field task allows for easier post-processing stitching of scans together and improving the quality of the data output. Well-placed reflectors, with consistent height, can allow for multiple scans over a large area. However if the target of interest is laterally extensive, reflectors can be moved from one side to the other in a technique called leap frogging, to continue to follow the quadrant rule.

After the equipment is set up, it is important to use a highly precise global positioning system (GPS) to record the position of reflectors and no less than three points to register the point cloud (collection of discrete reflection points in a computer system) into a Global Coordinate System (GLCS). Any lidar registration can be correlated to GPS coordinates; however it must be done carefully. Lidar data can have centimeter to even millimeter spacing, which is far more accurate than almost any publically available GPS systems (Bellian et al., 2005). It is desirable to take GPS readings, even if the project does not require it as future projects may require GPS data and without GPS coordinates; the point cloud would be rendered inadequate. A detailed procedure of scan set-up and acquisition is located in Appendix A (Field Steps).

3.2 Lidar Data Validation/Analysis

3.2.1 Validation by Manual Measurements

Fracture orientations and dips were measured using a Brunton© transit. Fracture measurements were plotted on lower hemisphere pole projections contoured by 1% area using Stereonet 9 software. All planes detected in the lidar data were validated by either manual measurements directly or, in cases where manual field measurements were not available, photos of the outcrop draped over the mesh for visual confirmation.

3.2.2 RiSCAN PRO

Data collected in the field were transferred to the RiSCAN PRO software for initial visualization. External hard drives are better to store lidar data due to the large size of the files, which commonly range from 2 gigabytes (GBs) to 10s of GBs. Once in RiSCAN PRO the GPS coordinates can be imported as a .csv file, in the format illustrated in Table 2, into tie-point list (TPL) GLCS and assigned tie points already found in the field. If tie points are not established

Reflector	**1**	**2**	**3**	**5**	**6**	**7**	**8**
Easting	670195.3	670213.5	670247.7	670303.3	670274.3	670227.6	670189.1
Northing	3772354	3772357	3772309	3772267	3772254	3772294	3772335
Elevation	258.485	257.508	255.763	256.427	254.679	257.153	257.29

Table 2 - Format used for importing GPS coordinates into RiSCAN PRO.

in the field, they can be determined off site as part of post processing. An important caveat, creating tie points anywhere besides in the field eliminates the possibility of correcting possible registration errors. Once the GPS coordinates are uploaded they must be moved to the Project Coordinate System (PRCS). To create the best overlaying fit, which means placing all the scan positions in the correct orientation to one another, each scan must find corresponding points in TPL SOCS (or Scanner's Own Coordinate System). Setting parameters such as tolerance of

possible locations in meters, and finding at least three corresponding points in other scans facilitate establishing correspondence.

Once completed for all scans, a multi-station adjustment can be used to eliminate any other possible separation in points. Multi-station adjustment for this thesis was done using the least square fit method (*personal communication*, Tan Nguyen, *RIEGL* USA, 2014). Once the point cloud has been registered, the photos captured can be undistorted to create a better fit on the point cloud, and then colored. Other cosmetic features such as the terrain filter or the deviation filter can be applied in RiSCAN PRO before exporting the point cloud. The terrain filter was used to remove vegetation from the point cloud by comparing reflection magnitude from a local zone and removing anomalous appearing reflections. A deviation filter was applied to eliminate data spikes. When two objects are less than 40 cm apart, the scanner tends to receive multiple returns between these surfaces creating a false spike. These data were then exported as a XYZ ASCII file from RiSCAN PRO to be used in Split-Fx engineering software. The I/O procedure is provided in detail in Appendix A (Exporting Scans as ASCII Files).

3.2.3 Split-Fx

Split-Fx software imports text files with UTM coordinates where X is easting, Y is northing and Z is elevation. Also, if a colored point cloud is imported, RGB data (red, green and blue points used to color the image), should be selected to color the image in Split-Fx. Large point clouds with tens of millions of points tend to require lengthy loading times and if colored movement of the point cloud can lag substantially. After importing the point cloud, a mesh was created by use of the triangulation method; ten-point spacing per triangle was used for all the meshes. However, the triangulation is data dependent. If there are large holes (zero-reflection zones) in the data, larger point spacing may enable better triangulation.

Based on the similarity of the dimension and orientation of the mesh triangles, the triangular elements are then combined into groups, hereafter referred to as "patches." These patches represent surfaces in the mesh, including fracture planes, bedding surfaces, the outcrop surface, etc. Fractures were identified by large groupings of similar poles in the patch generation called sets in conjunction with known orientations from the hand-measured fractures. The user, to ensure that the outcrops appearance is honored, can control patch creation. An automated feature in Split-Fx that allows minimum patch size and neighboring angles to be adjusted can also create patches. In this application, a minimum patch size of 5 mesh triangles and a maximum neighbor angle of 12^0 were used. The software automatically measures the strike and dip of individual patches. In this application, user-defined polygons hereafter referred to as "traces" were used to differentiate between automated and hand-picked fracture planes. Like for the patches, the software can also measure the strikes and dips of the traces. Patches and traces can be exported from Split-Fx in text files containing strike and dip measurements. In this application, the exported strike and dips were used to recreate the fracture plane and visualize them in a lower area hemispherical projection stereonet. Details of the plotting and exporting procedure are provided in Appendix B.

3.3 X-Ray Diffraction (XRD) and Thin Section Analysis

Samples were collected in the McAlister Shale Pit from locations representing the upper, middle and lower sections of the Woodford Shale. A total of 30 samples were collected for XRD analysis. These samples were selected, based on both accessibility and adequate representation of the section face. These samples were collected at an adequate depth below the surface (typically 10 to 15 cm) to reduce the impact of weathering on mineral composition. Once collected, samples were stored in labeled Ziploc© plastic bags. In the lab, samples were powdered and placed in sample trays for XRD analysis. X-ray diffraction is a common analytical technique for the study of crystal structures and phase identification of crystalline material. It works by producing x-rays

that are scattered or diffracted by the mineral's crystal lattice to produce characteristic x-ray spectra based on Bragg's Law (Scintag, 1999).

XRD analysis of powdered samples was used to established bulk mineralogy, 2-theta angles 0 to 75 (Chipera and Bish, 2013). 2-Theta angles represent the diffraction angle of the reflection. For analysis of clay in the samples, the powdered samples were first placed in test tubes with sodium acetate, then stirred and heated to 80˚F, and centrifuged. The liquid was decanted and the process was repeated until clay formed a visible suspension. The clay was collected with a pipette and placed on a glass slide to form a clay smear, which when dried, was x-rayed.

Besides preparing the hand samples for XRD analysis, 14 samples were thin sectioned. XRD data were integrated with thin section analysis to identify the mineral composition of the Woodford Shale. Thus, thin section analysis was used as a framework to interpret the XRD scans. An example in provided in Appendix C (Thin Sections and XRD Comparison), where gypsum occurs as fracture-filling cement that was first detected in thin section and then interpreted in the XRD scans. For all 30 samples, the XRD diffraction patterns were analyzed and peaks matched to their mineralogical counterparts to create a semi-quantitative characterization of mineralogy.

CHAPTER IV

RESULTS

4.1 Validation using Field Data

Forty strike and dip measurements were made in the upper section using a Brunton© transit (Figure 8A). The intent of manually collecting field data was to confirm the veracity of lidar-derived (Figure 8B) measurements of extracted strike and dips (e.g., Figure 9). The manual strike and dip data were visualized in the form of lower hemisphere equal area pole projections (Figure 10A). Presentation of both manual and lidar data in this manner enabled interpretation of the dominant bedding and fracture plane orientations from clusters of poles in the stereonet. Four dominant pole clusters could be identified. The cluster with an average strike N29˚W and average dip 36˚NE is the bedding plane (Label D; Figure 10). By default, all other pole clusters are assumed to be representing fracture planes. The cluster with an average strike N30˚E and dip 50˚NW is labeled A. The cluster with average strike N20˚W and dip 41˚SW is labeled B, and cluster C has an average strike of N50˚E and near-vertical dip.

Similarly, forty-six strike and dip measurements were made in the middle section of the Woodford Shale (Figure 11A). Like in the upper section, the intent was to check the fidelity of the lidar data as well as the robustness of processing algorithms (Figure 12). Similar to the upper section, the field strike and dip data were visualized in the form of lower hemisphere equal area pole projections (Figure 13). As with in the upper section, four dominant pole clusters could be identified in the middle section. The cluster with an average strike N40˚W and clusters could

be identified. The cluster with an average strike N40˚W and an average dip 39˚NE is interpreted as the bedding plane. The cluster with an average strike N34˚E and an average dip 50˚NW is interpreted as Set A. Set B has an average strike of N10˚W and an average dip 47˚SW, whereas Set C has an average strike N72˚E and an average dip 76˚SE.

In both the upper and middle sections, hand measurements were limited to dominant and systematic sets only. For the upper section, site accessibility proved to be a limiting factor in being able to sample all possible fracture sets even after visually locating them. Although the bedding and dominant fracture planes were similar in the upper and the middle Woodford, the weathering patterns were different. The upper section is weathered more in the fissile beds associated with phosphate nodules. As a result, the upper section was characterized by protruding chert beds. The middle section is weathered more uniformly. The difference in weathering did not affect the hand-measurements, which were guided by visuals, but affected automated interpretation of the lidar data. No kinematics deformation indicators such as slickensides were seen either in the upper or the lower section; as a result the field data could not be related to paleostress directions.

4.2 Lidar-Based Model Development

The relief and exposure as a result of quarrying allowed lidar observations to be made in both bedding perpendicular and bedding parallel views (Figure 8, upper; Figure 11, middle). Triangulation followed by guided picking (Appendix B) resulted in 9,404 discrete patches. Anomalous patches (caused by vegetation, debris, etc.) from algorithmic misinterpretation or registration of the point-cloud were deleted resulting in ~5% decrease in total patch count. In principle, each patch is representative of a plane (which a strike and dip value). Lower hemisphere equal area pole projections for all the patches were made in Stereonet 9 software. The clustering of the poles, much like in the had-picked case, was used to judge the overall geological

sensibility of the results. Field and lidar stereonets were compared for each section (Figure 10: upper; Figure 13 middle).

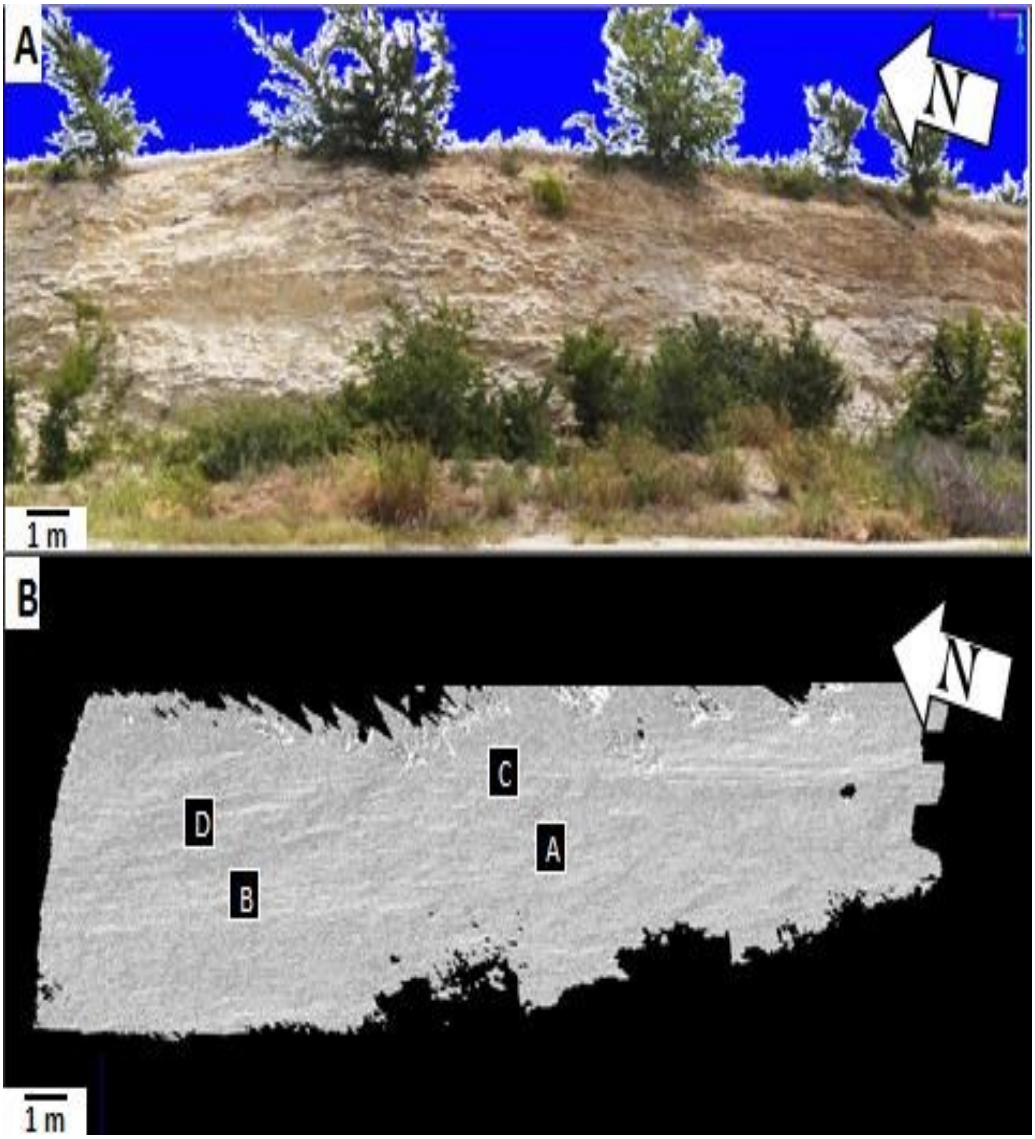

Figure 8 – Upper section image and mesh. (A) High-resolution colored scan of the upper section, where hand-measurements were taken at the McAlister Shale Pit in RiSCAN PRO. (B) Representation of (A) as triangular mesh in Split-Fx (software used for fracture analysis; see text for details). In (B) the labels A-D represent the locations of fracture images provided in Figure 9.

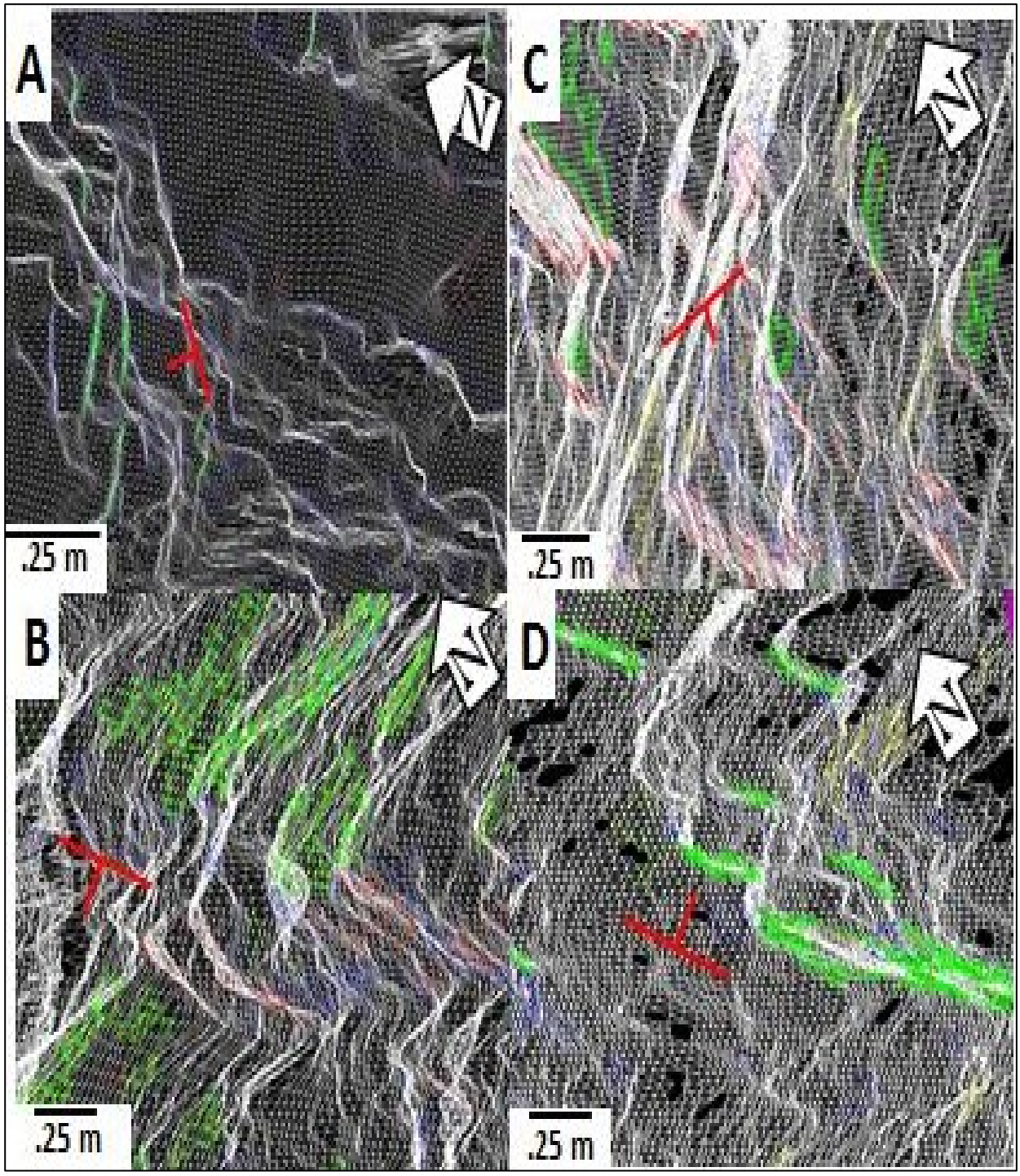

Figure 9 – Fracture interpretation in Split-Fx for the upper section. The interpreter specifies criteria for a fracture plane (minimum patch size, maximum neighbor angle and point filter) which then is used as a guide by the software for picking fractures throughout the sample space. (A) Manually created polygons to interpret a fracture set striking NE and dipping NW, which could not be identified in the lidar data using the procedure above. (B) Set highlighted perpendicular to (D) representing fracture striking NW and dipping SW. (C) Set highlighted represents fracture striking ENE and dipping SSE. Although photographed, these fractures could not be measured in the field due to access difficulty. (D) Set highlighted represents the bedding plane, which strikes NW and dips NE.

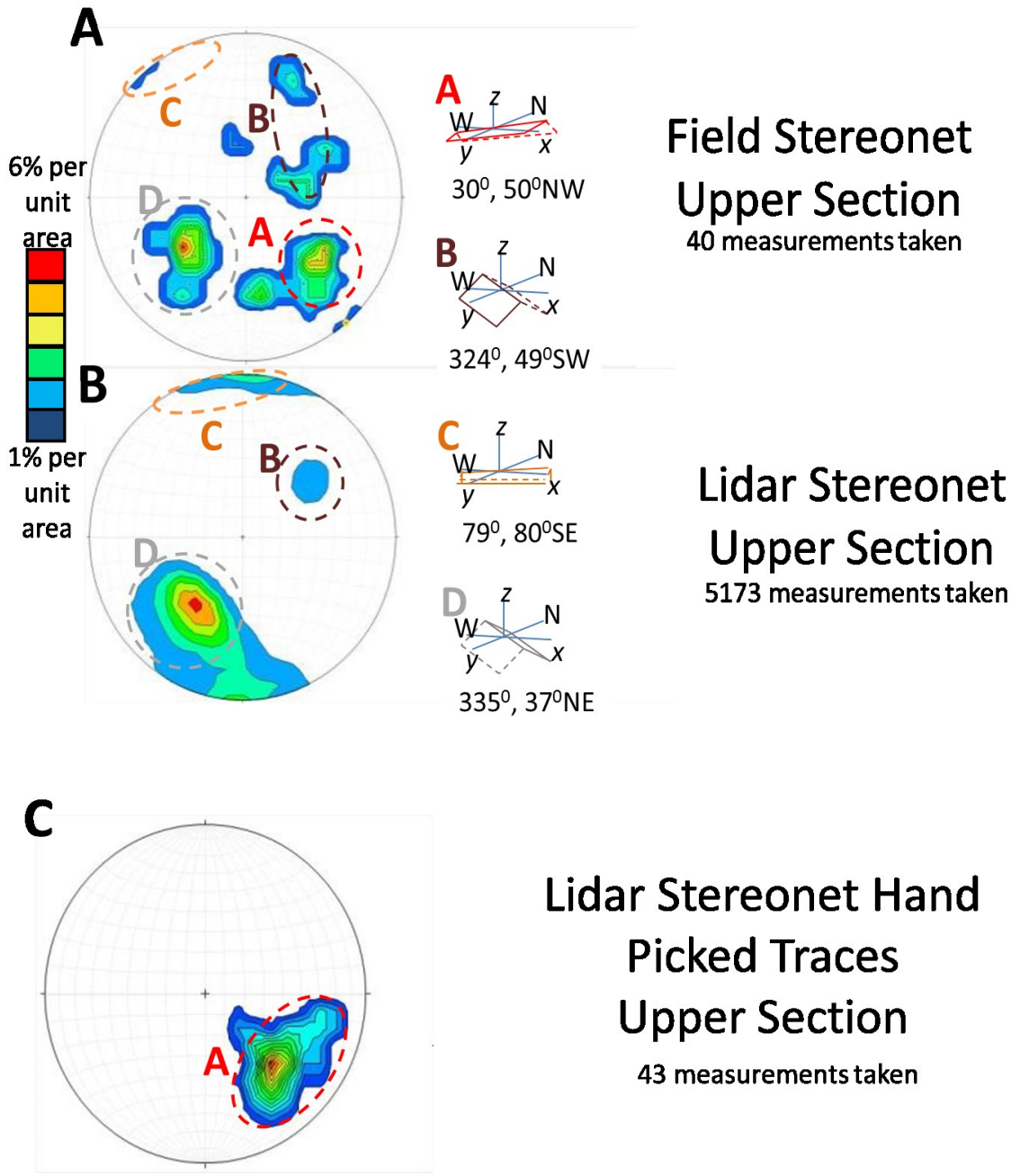

Figure 10 – Lower hemisphere stereonets for the upper section. (A) Manual measurements, (B) lidar data automated interpretation and (C) lidar data manual interpretation of selected fracture planes (see text for details). In (A) – (C) The poles to the (fracture and bedding) are contoured in color with red representing higher and blue lower data density respectively. Label D represents poles for the bedding plane (corresponding to Figure 9A); labels A-C represent poles for fracture planes corresponding to Figures 9A – C.

4.2.1 Upper Section

The exposure of the upper section was near vertical and striking nearly N-S with a relief of ~11m (Figure 8A). The point cloud from lidar was converted to a representative mesh through triangulation (Figure 8B). The mesh was used for software guided; automated patch creation (Figure 9) and the corresponding poles were plotted on the stereonet (Figure 10). Three dominant pole clusters were observed in Figure 10B. The cluster with an average strike N25˚W and an average dip 37˚NE was interpreted as the bedding plane. Clusters with average strike N36˚W and N79˚E and corresponding average dip 49˚SW and 81˚SE respectively, were interpreted as Set B and C fractures. Patches corresponding to Set A could not be automatically created in the software, because these fractures failed to meet the criteria by the algorithm method for patch generation. However, these fractures could be visually identified in the mesh and corresponding hand-picked patches could be created. Set A poles are also presented in Figure 10C.

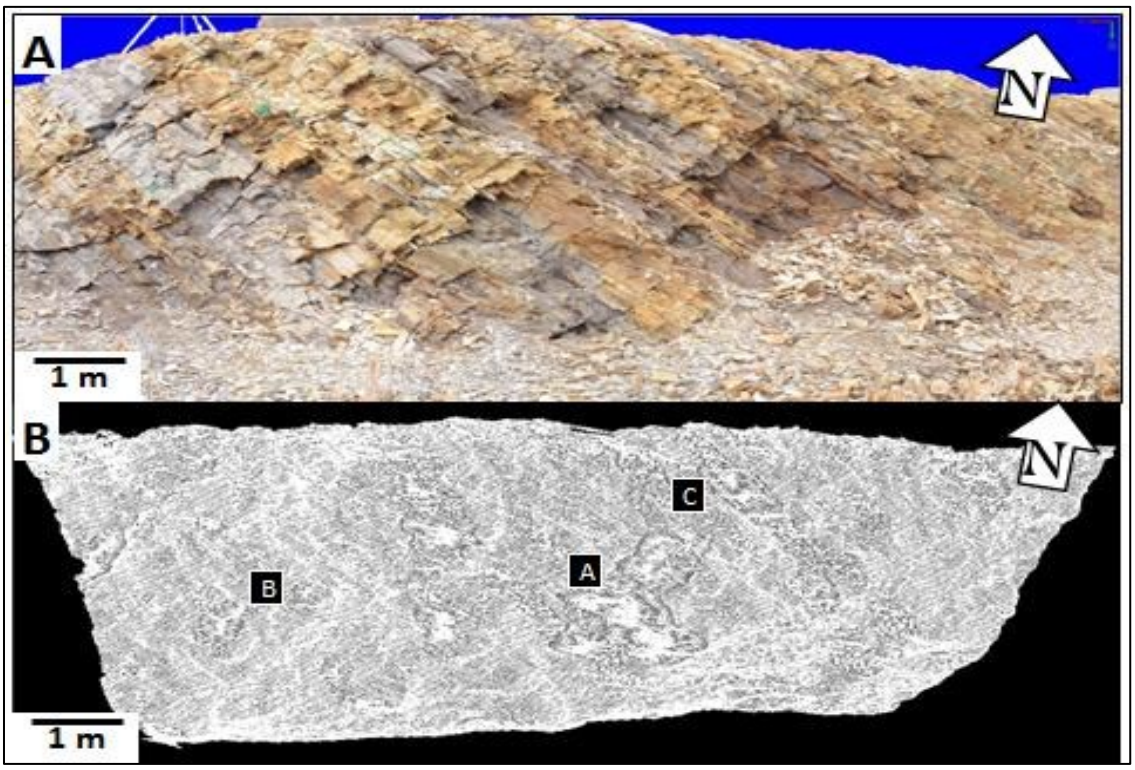

Figure 11 – Middle section image and mesh (A) High-resolution colored scan of the middle section, where hand-measurements were taken at the McAlister Shale Pit in RiSCAN PRO. (B) Representation of (A) as triangular mesh in Split-Fx (software used for fracture analysis). In (B) the labels A-C represent the locations of fracture images provided in Figure 12.

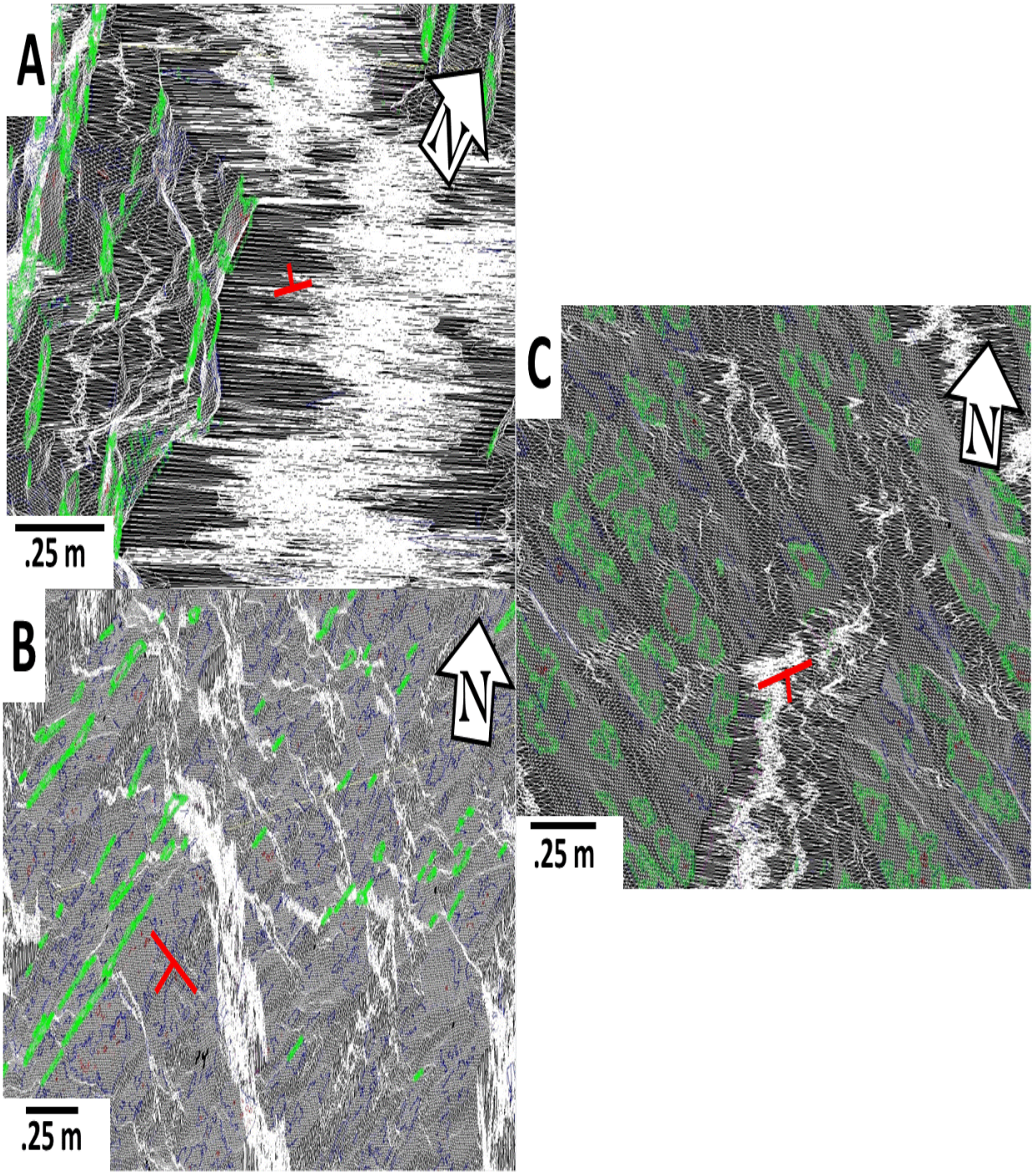

Figure 12 - Fracture interpretation in Split-Fx for the middle section. (A) Representing fractures striking NE and dipping NW; (B) Set highlighted represents fractures striking NW and dipping SW; (C) Set highlighted represents fracture striking ENE and dipping SSE.

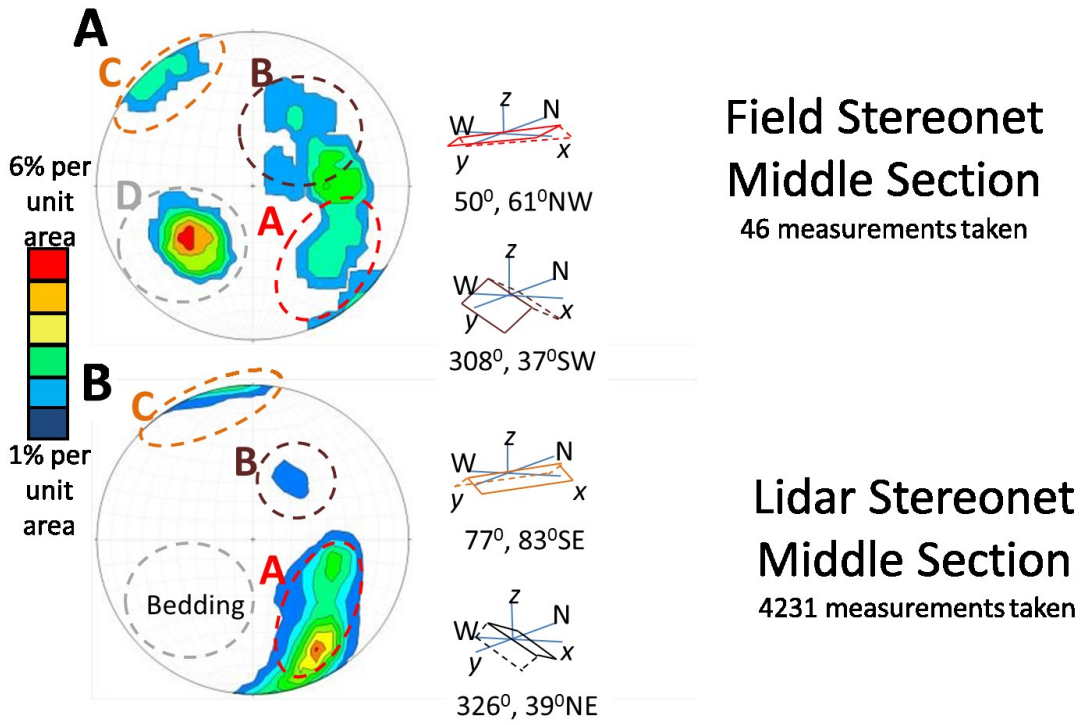

Figure 13 – Lower hemisphere stereonets for the middle section in the Woodford Shale. (A) Manual measurements, (B) lidar data automated interpretation. In (A) and (B) the fracture planes poles are contoured in color with red representing higher and blue lower data density, respectively. Labels A-C represents poles for fracture planes corresponding to Figures 12A-C.

4.2.2 Middle Section

The middle section strikes NE-SW and has approximately ~4m of relief (Figure 11A). This section allowed limited lidar and field work to be established. The point cloud from lidar was converted to a representative mesh through triangulation (Figure 11B). The mesh was used for software guidance and automated patch creation, (Figure 12) and the corresponding poles were plotted on the stereonet (Figure 13B). Three major pole clusters could be identified. Clusters with average strike N56˚E, N55˚W and N77˚E and corresponding average dips 61˚NW, 37˚SW and 83˚SE were respectively interpreted as Set A, B and C fractures. The discrepancy between the field and lidar stereonets was much less in the middle section compared to the upper section.

4.3 Lidar Intensity vs. Gamma Ray

Besides the spatial data recorded for a scan acquisition, lidar also records reflection intensity, which in principle contains information on the chemical make-up of the reflecting surface. Traditionally, gamma-ray curves have been used to remotely sense the amount of uranium, thorium and potassium in the surveyed interval. A comparison of total gamma-ray value with lidar intensities in both the upper and middle sections was conducted in the areas surveyed previously with the spectral gamma-ray (Figure 14). A gamma-ray curve and lithology weathering profile (*personal communication,* Jim Puckette, 2013) is shown in Figure 15, and areas of lidar investigation are highlighted. When total gamma-ray values are plotted against lidar intensities, a reciprocal relationship is suggested for both the upper (Figure 16) and middle (Figure 17) sections of the Woodford Shale. To decipher this observed inverse relationship between lidar intensity and mineralogy as indicated by gamma-ray values (e.g., Burton et al., 2011); representative samples were selected for x-ray diffraction (Figure 18). The x-ray diffraction results appear to indicate that while clay minerals that are associated with higher gamma-ray values cause a decrease in lidar intensity, quartz associated with low gamma-ray values can increase lidar intensity. A cross plot of lidar intensity with gamma-ray values illustrates the inverse relationship (Figure 19).

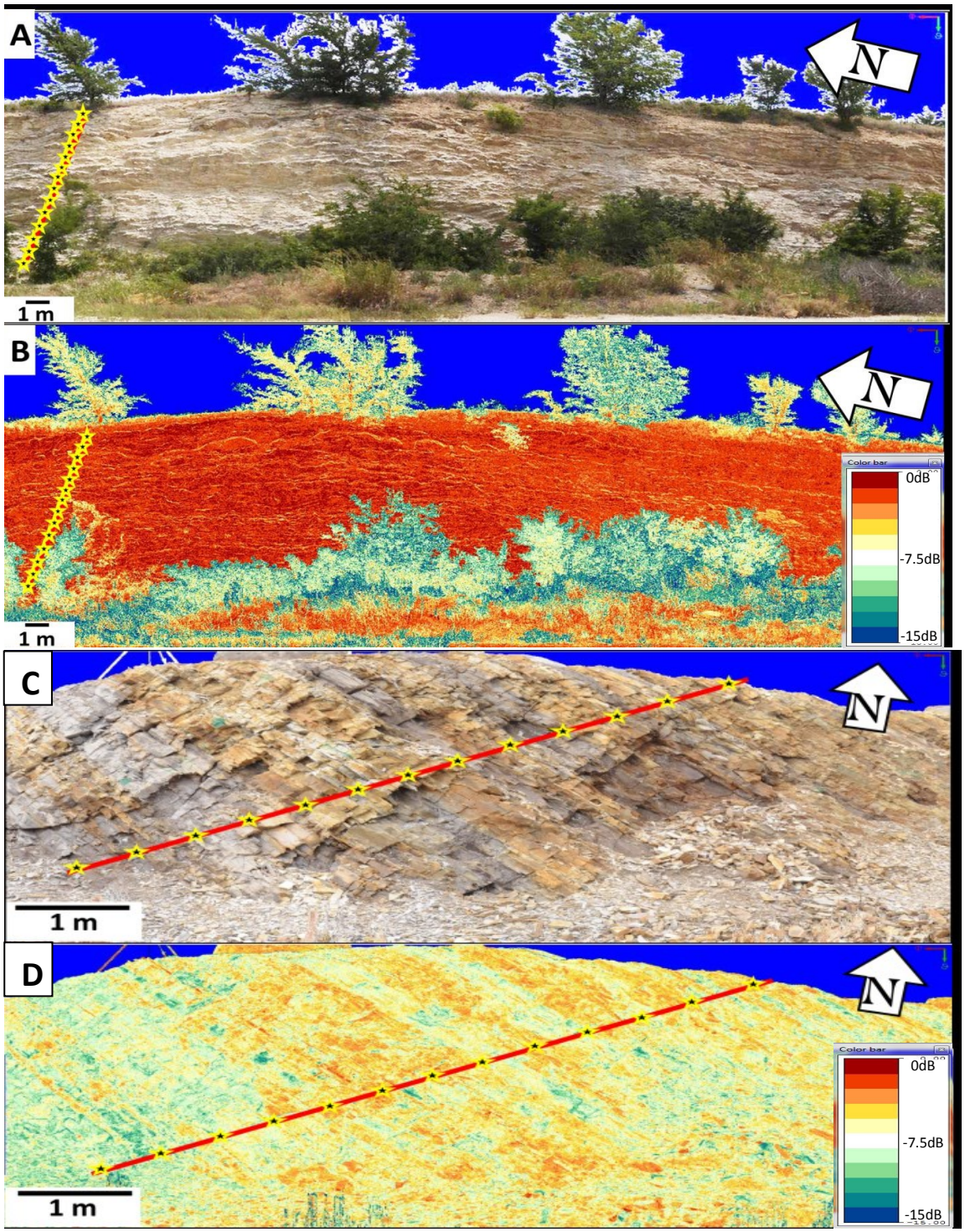

Figure 14 – Measured sections for gamma-ray and lidar intensities. (A) High resolution colored scan and (B) intensity display in decibels for the upper section. (C) High resolution colored scan and (D) intensity display in decibels for the middle section. In (A) – (D) the location of the gamma-ray profile is marked in solid stars. Intensity is the amount of energy reflected from the surface under observation. Color intensities in Figure 14B and D suggest that the upper section has higher intensity, which could be due to higher quartz content in the upper section compared to the middle section (C and D).

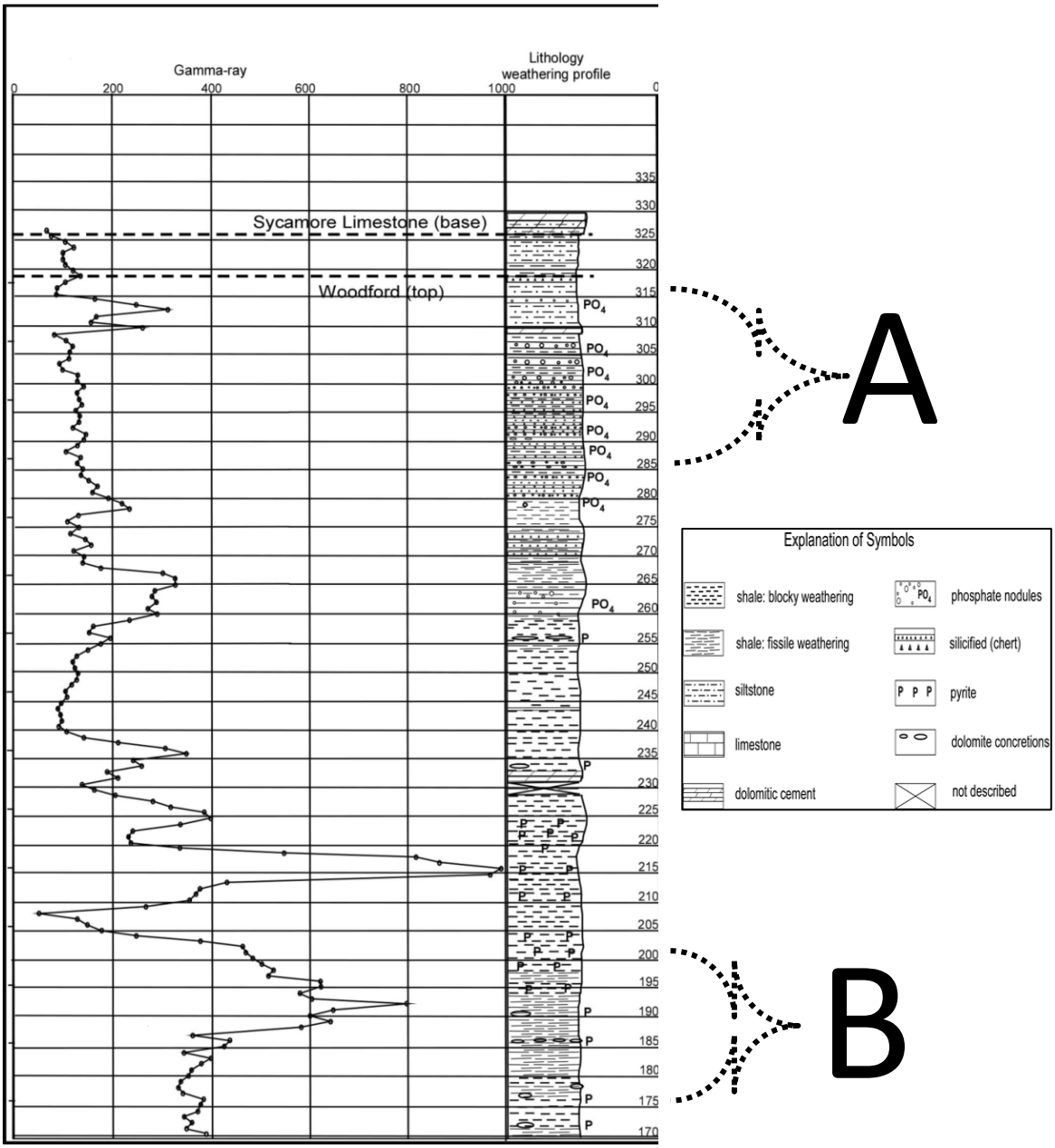

Figure 15- Gamma-ray (GR) curve and lithology profile from upper and middle sections of the Woodford Shale (after Puckette et al. 2013). Lidar intensity is compare with SGR and lithology in Sections A and B.

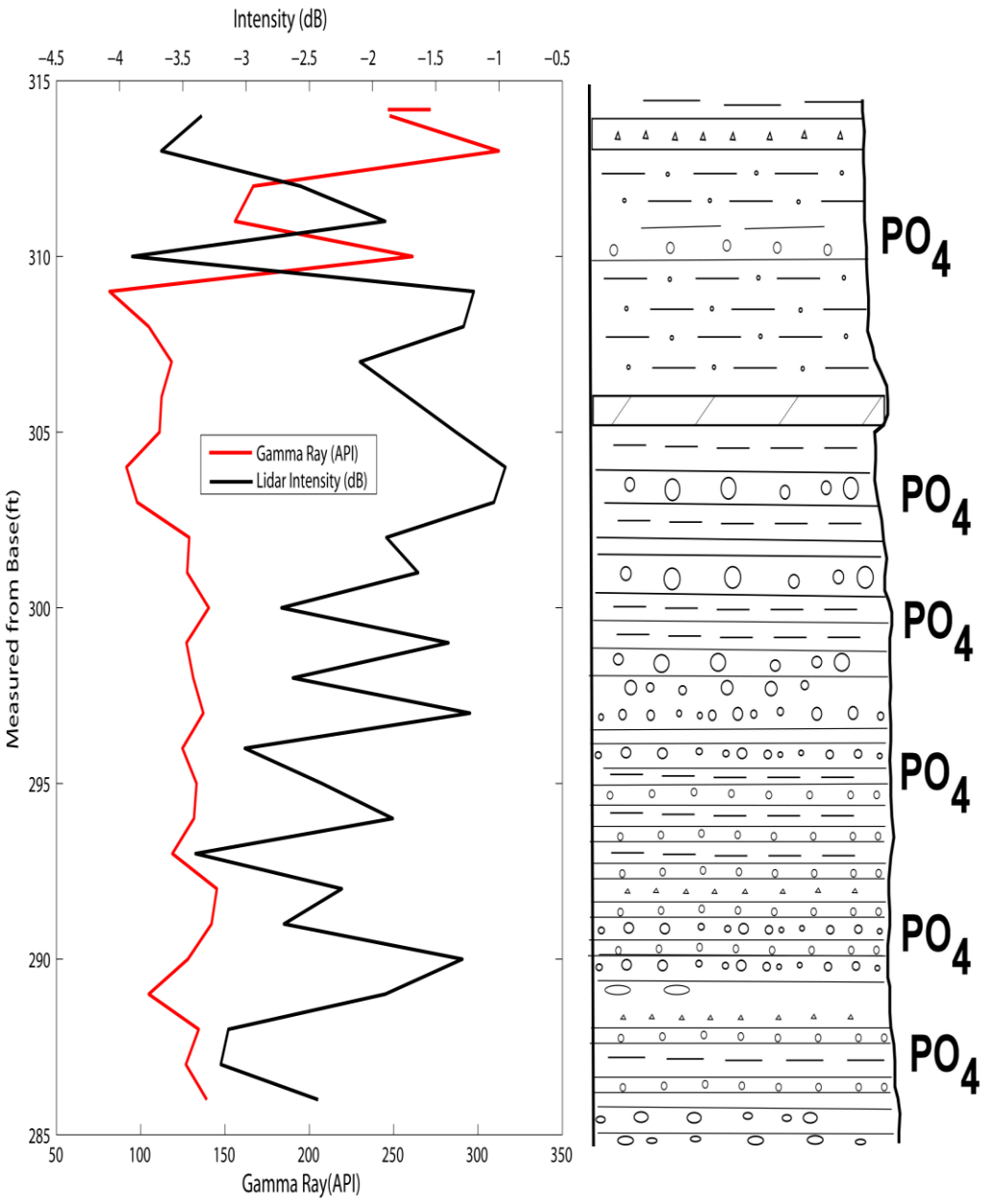

Figure 16 – Gamma-ray values versus lidar intensity plot for the upper section of the Woodford Shale. This plot indicates an inverse relationship. A lithology profile is located to the right of the plot (Modified Puckette et al. 2013). A description of the symbols can be found in Figure 15. Increased quartz concentrations lead to decrease gamma-ray readings and increase intensity signatures.

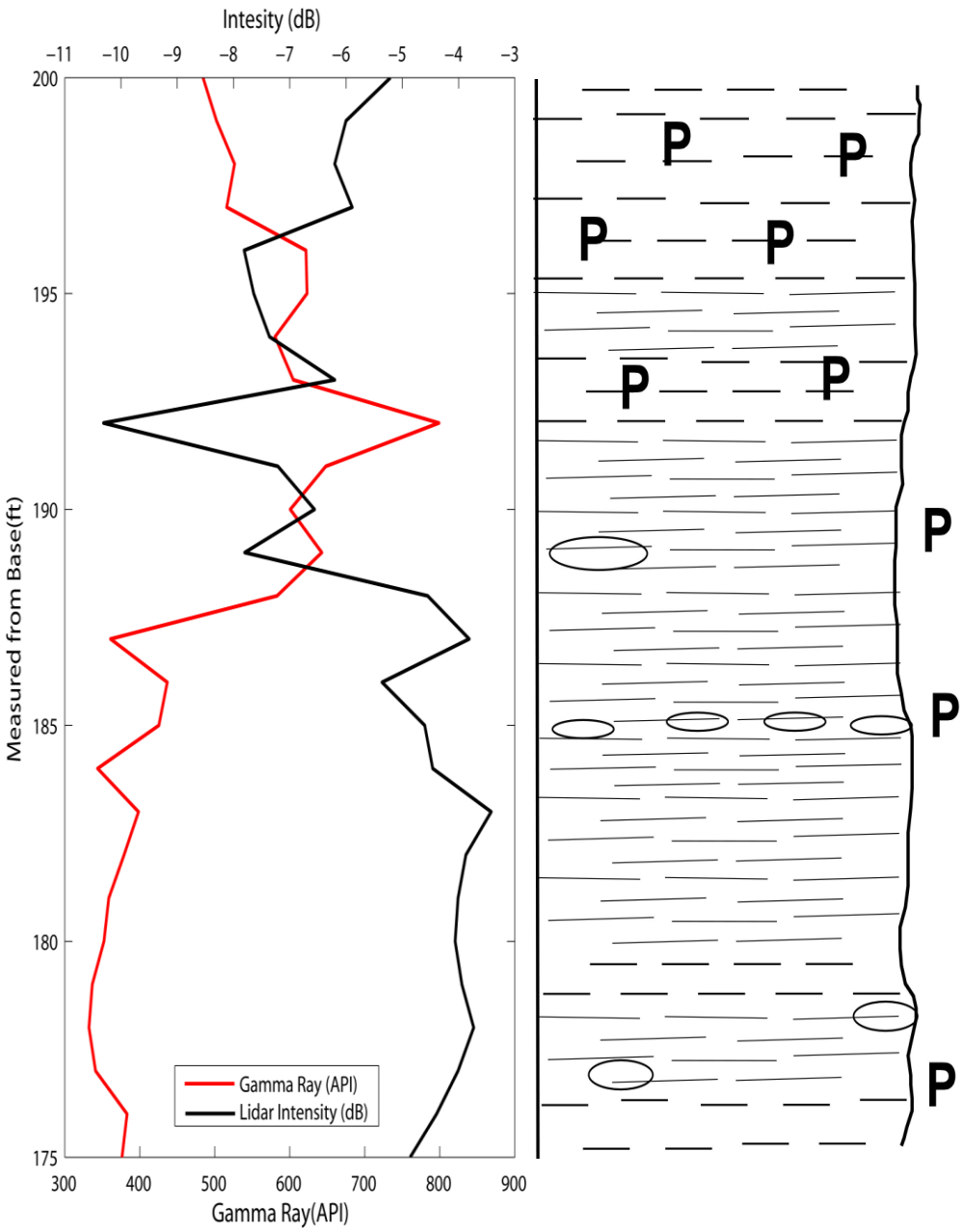

Figure 17 – Gamma-ray values versus lidar intensity plot for the middle section of the Woodford Shale. This plot indicates an inverse relationship. A lithology profile is located to the right of the plot (Modified Puckette et al. 2013). A description of the symbols can be found in Figure 15. Lidar intensity decreases with increasing concentrations of illite, chlorite, and other clays, which tend to increase gamma-ray values.

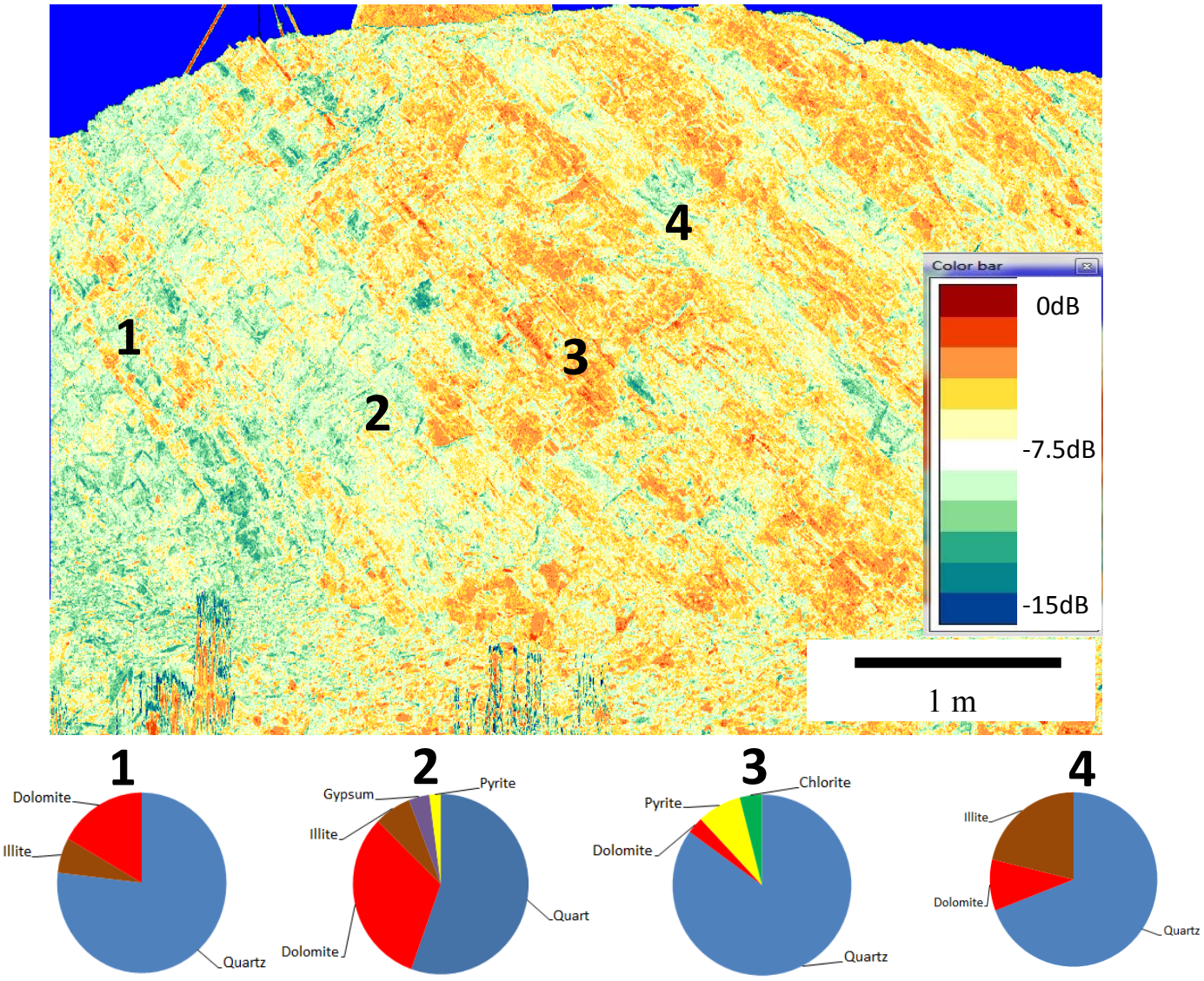

Figure 18 – Scan of the middle section under reflectance filter, measured in decibels, showing reflectance heterogeneity between beds. Numbers represent the location of XRD sample locations. Associated with each number, is a semi-quantitative pie chart for analyzed XRD scans. Intensity values increase with higher quartz values on the semi-quantitative charts. The blue coloring in the upper most part of the figure represents no laser reflected back and not very low intensity.

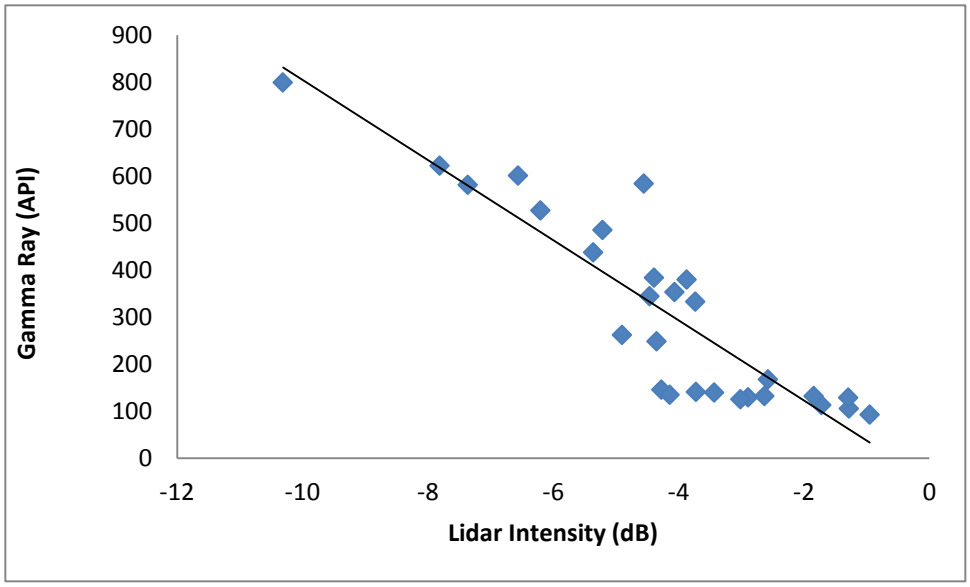

Figure 19 – Cross plot of gamma ray readings against lidar intensities to show the inverse relationship (r = -0.89).

4.4 Linear Fracture Density – Model Development and Validation

Fracture densities in the Woodford Shale were measured along profiles perpendicular to the bedding plane. Similar to field lines, virtual scanlines were created using the lidar mesh by rotating the point cloud along the strike and measuring the distance between the individual patches. To confirm the fidelity of virtual scanlines, linear fracture densities were hand-measured along the path of the virtual scanlines, which confirmed that lidar-derived and hand-measured fracture densities were similar. Following these measurements linear fracture density was computed with confidence along a number of additional virtual scanlines in the upper and middle sections.

Using measurements from the scanlines field checked by hand measurements as well as those from the virtual scans as visualized on Split-Fx, a scatterplot was created with fracture density (number of fractures divided by fracture spacing) along y-axis and bed thickness along the x-axis (Figure 20). The distribution of data in the graph is interpreted to make the inference that for non-fissile beds, fracture density decreases with increasing bed thickness. Figure 21 also

suggests that the upper section has less variance from fracture to fracture than in the middle sections.

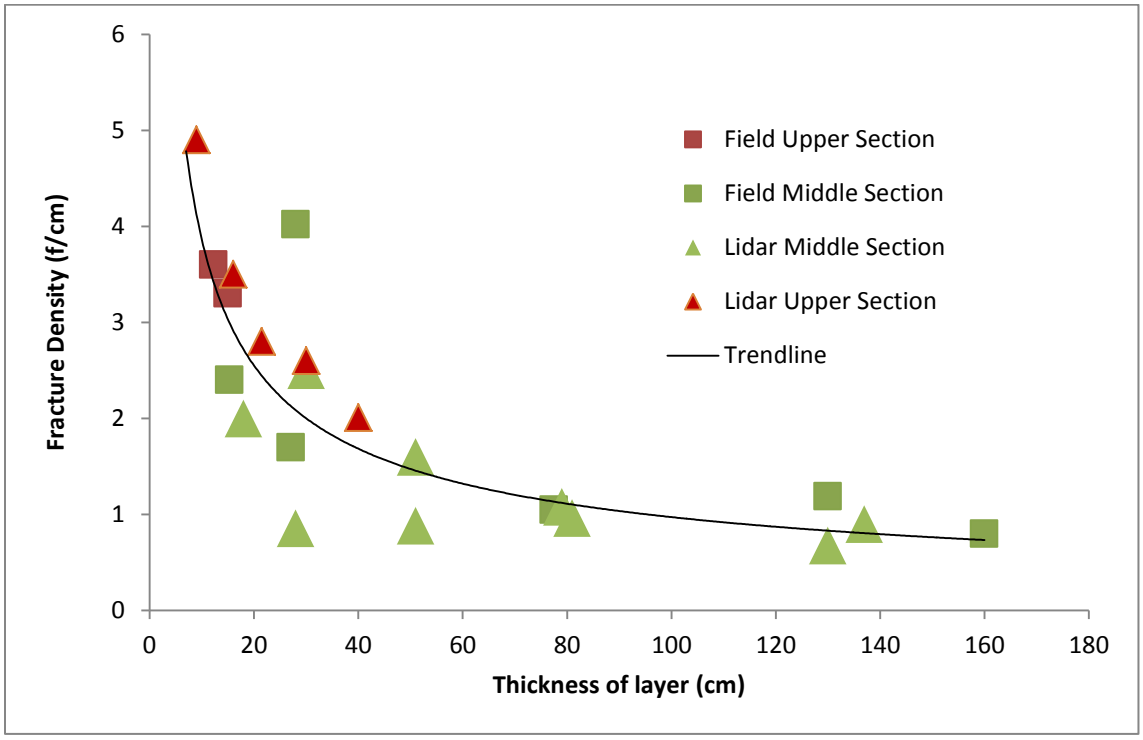

Figure 20 – Linear fracture density versus bedset thickness for non-fissile beds. Data distribution shows that thinner beds have a higher density of fractures (r = 0.81).

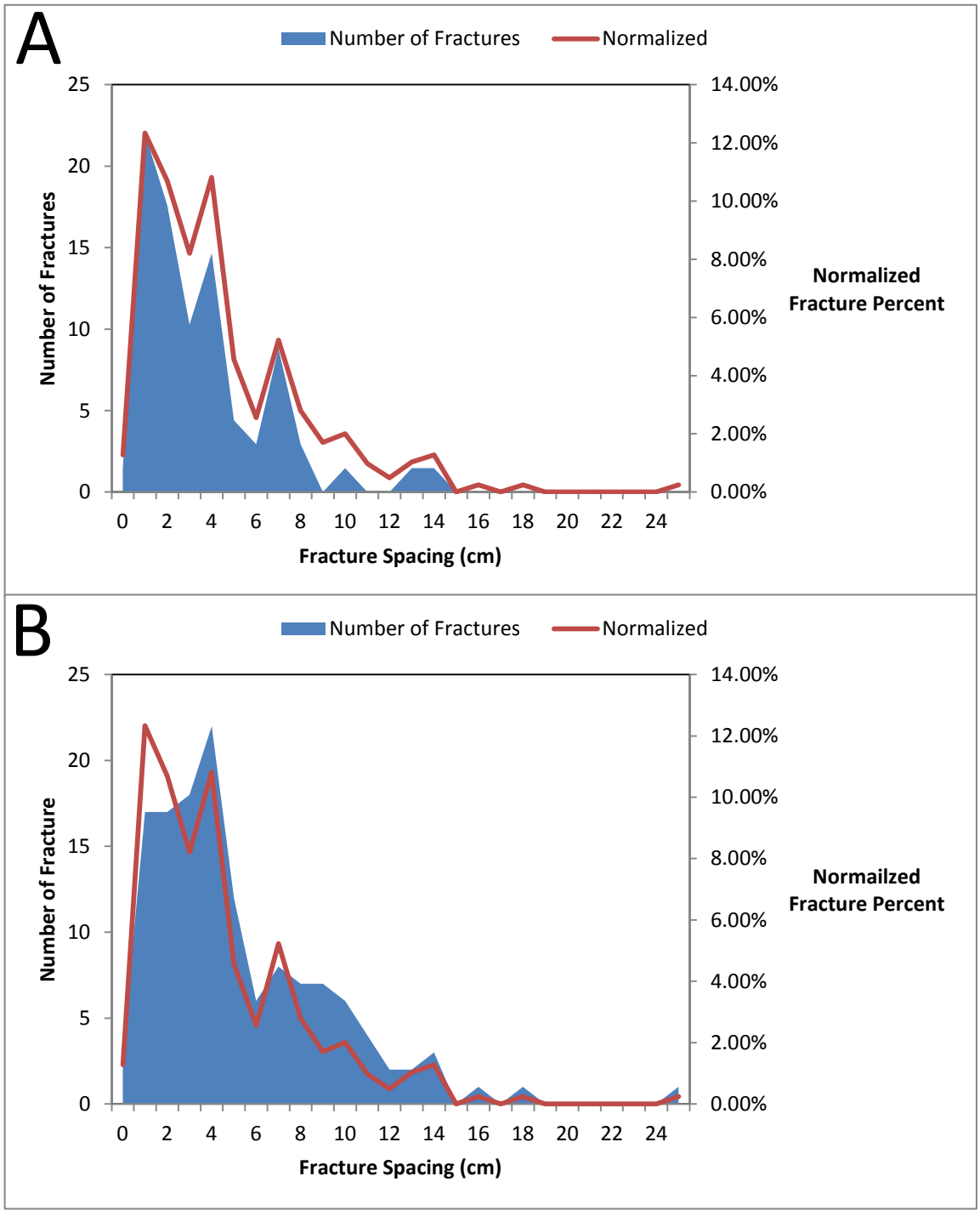

Figure 21 – Fracture spacing along NW-SE profiles (perpendicular to the dominant fracture strike direction) in (A) upper Woodford section (B) middle Woodford section. Fracture spacing refers to the distance between two adjacent fractures. In (A) and (B) the normalized curve includes data from all sections. Examination of these distribution patterns resulted in the inference that fractures in the middle section have a larger spacing than fractures in the upper section.

CHAPTER V

DISCUSSION

5.1 Lidar Effectiveness in Fracture Mapping

As opposed to cognitive processes that identify a fracture based on subtle differences in the appearance (color or texture) of the rock face, lidar relies on morphology, i.e., subtle differences in relief that occur in the fractured zone with respect to the background rock face. Different weathering patterns in the upper and middle sections with respect to the viewing angle or surveyor's perspective appear to influence ease of identification/recognition. For example, Set A fractures in the upper section of the Woodford Shale could not be readily identified in lidar data. This discrepancy is likely due to a more uniformly weathered surface across the middle section of the Woodford Shale. The surface topography of the middle section was gentler than the upper section, which allowed the automated patch creation algorithm to work more efficiently. From a mapping perspective the middle section of the Woodford Shale at the McAlister Shale Pit was ideal for lidar-based fracture analysis.

Unlike the upper section, the bedding planes were not readily detectable in the middle section. This phenomenon is attributed to the less pronounced differential weathering in the middle section. The upper section has resistant chert beds immediately overlying fissile beds. The fissile beds weather at a more frequent rate than the adjacent chert-rich beds, resulting in chert bed ledges that stand out both visually as well as in the lidar data set. In both the upper and middle sections, Set B (N55˚W, 37˚ SW) dips at a right angle to the present attitude of the

bedding plane. Set A and C appear to be conjugate sets, which was also suggested by Ataman (2008). Sets A and B are more systematic than set C. Although the manually acquired field data have a larger uncertainty, the results can be correlated with lidar results. In addition, thin section examination found fractures subparallel to bedding. These micro-fractures are not apparent at outcrop scale.

Hypothetically, if the face of the rock is completely flat and smooth with fractures appearing as pencil thin lines on the surface, interpretation of the lidar point-cloud data could not be automated to pick fractures. Thus, an argument can be made that it is the (differential) weathering of the rock that creates the morphology required by lidar for mapping. Needless to say, rate of weathering depends on many factors, including climate, rock composition and aspect. Rocks of different composition will weather differently under the same ambient conditions (precipitation, slope and temperature). In a small study area, such as the McAlister Shale Pit, the rocks surveyed are exposed to similar ambient conditions and have similar aspect. The original argument can be further extended to say that it is the subtle difference in mineralogy that generates the features mapped by the lidar.

Spectral attributes of the data collected by lidar can help determine rock composition. The spectral attribute refers to intensity, which is the return strength of the laser pulse (which in turn is a function of the wavelength - near-infrared in this thesis). Beyond weather or moisture conditions, intensity is somewhat independent of reflection distance. The biggest benefit of this attribute to this study is its potential linkage with mineralogy. At the McAlister Shale Pit, an inverse relationship between lidar intensity and total API gamma-ray is apparent. Although this relationship is not perfectly reciprocal, XRD analysis of selected samples shows that radiogenic minerals, such as clays, which enhance gamma-ray signals, appear to increase in beds with diminishing intensity. Thus beds with increased clay content, are expected to contain water bound to the clay structure, and as a result lidar intensity is impacted. Simultaneous analysis of both attributes provides as to for the inability of lidar to map bedding planes in the middle section of

the Woodford Shale. Lidar intensity shows more variation in mineralogy in the upper section than the middle section, which in itself could impact rate of weathering and result in the differential patterns that improve definition in the bedding planes. Burton et al. (2011) reported that intensity was related to the physical and chemical properties of the reflecting target and this study affirms those findings.

5.2 Lidar Error Sources

In this thesis, the lidar point cloud data were converted into a mesh by gridding and triangulation. This is taking advantage of the spatial attribute of the data. Following conversion, mesh attributes such as size and orientation of the individual triangles were used to group them into individual patches, which could be interpreted as independent (bedding or fracture) planes. Finally, lower-hemisphere equal-area pole projections on stereonets were used to visualize the strike and dip of patches. In order to compare these results with other field data the GPS registration is the most critical element in data acquisition (Bellian et al., 2005). Multiple scans were required for completion. The oldest vintage data, due to errors in GPS registration, did not yield geologically sensible results. Registration error does not allow individual scans to be spliced together. A multi-station adjustment is feasible for correction if the error is minimal. Another error source and limitation is geospatial. It originates because GPS readings are not precise enough to position the individual reflection points in the data cloud. This limitation can be and was overcome by taking multiple GPS readings. Multi-station adjustment mitigates this limitation as well.

5.3 Mineralogy and Fracture Characteristics

Some generic observations on the relationship of mineralogy to fractures are presented. Fractures observed in silica-rich beds often terminated within the organic-rich beds and few fractures propagated within organic-rich beds. Units with more brittle constituents such as quartz

were found to have a larger fracture density. This indicates that while organic-rich units better accommodate stress, strain partitioning is better in the silica-rich beds.

Besides mineralogy, thickness affects fracture density as well. Thicker units had low fracture density than thinner units with the exception of fissile and thinly laminated beds. Regardless of their thickness, in response stress loading, these units split along the bedding planes causing low fracture densities. XRD results show that fissile beds have lower quartz content relative to other minerals than adjacent more blocky beds. Fissile units are composed of alternating laminae of clay, organic material and quartz that form tabular flat-lying laminae; due to a lack of vertical bonding, the laminae separate due to stress relief and/or weathering. Thin-section analyses also revealed that the organic-rich and fissile beds have bedding parallel micro-fractures. These fractures are cemented in some cases, evidence that they are a natural phenomenon and not mechanically induced during thin sectioning.

XRD results from both upper and middle sections suggest that bulk mineralogy may not affect orientation of the systematic fractures on the scale of interpretation in this research. However, the non-systematic fractures appear to be increasing with the presence of minerals such as illite, chlorite and sulfides. Computation of linear fracture densities, in both field setting and in lidar dataset, suggested that rock composition can have a strong influence on fracture frequencies and spacing; the upper section with more quartz has more closely spaced fractures.

CHAPTER VI

CONCLUSIONS

Lidar data were used for inferring strike and dip of (bedding and fracture) planes in the upper and middle sections of Woodford Shale outcrop in the McAlister Shale Pit, south-central Oklahoma. A stereonet based comparison between manual field measurements and lidar data strongly suggests that lidar could be used to map outcrop fractures in the Woodford Shale with confidence using the processing method presented in this research.

Three dominant fracture sets, perpendicular and oblique to the bedding plane, were found in the Woodford Shale of the McAlister Shale Pit using/based on both the hand-measured and the lidar data. In general, the fracture orientation is consistent with the paleo-stress regime of the southern Oklahoma. In this thesis, they are referred to as Set A (average strike and dip: $N41^0E$ and $54N^0W$ respectively); B (average strike and dip: $N30^0W$ and 44^0W respectively); C (average strike and dip: $N73^0E$ and 81^0SE respectively). Set A fractures could not be readily identified in the lidar data from the upper section of the Woodford Shale. On the other hand, bedding plane (average strike and dip: $N31^0W$ and 35^0NE respectively) could not be identified readily in the lidar data from the middle section of the Woodford Shale. Different weathering patterns for the upper and middle sections with respect to the viewing angle appear to be the reason for these differences.

A comparison between gamma-ray values (API units) and lidar intensity suggest a reciprocal relationship. XRD analysis of representative samples show that both gamma-ray and

lidar intensities are affected by the same minerals, but in opposite ways. Results strongly suggest that lidar has the potential to be used not just to image surface textures, but also as a possible proxy for composition. XRD results from both the upper and middle sections of the Woodford Shale suggest that bulk mineralogy may not affect orientation of the systematic fractures on the scale of this research. Computation of linear fracture densities from manual field measurements and the lidar data set, suggested that mineralogy can have a strong influence on fracture frequencies and spacing; the upper section with more quartz has more closely spaced fractures.

6.1 Future Work

The results of this study have implications for extrapolation of outcrop observations to the subsurface. The recognition that fractures frequency increases in thinner beds with high lidar intensity quartz-rich beds may help explain why relatively quartz (chert) poor mudrocks with silica enrichment at the laminae scale produce large volume of fluids. The orientation of fracture patterns evident in the studied outcrop may be an analog for subsurface orientations once those fractures likely formed by dilation from unroofing are removed from the set.

Detailed analyses of well planning that consider fracture orientation and placement of wellbore trajectories is lacking in literature. Outcrop studies such as this can offer important insights into the subsurface geomechanics and could be especially applicable in the Woodford Shale or compositionally similar rocks. The middle section of the Woodford Shale in the McAlister Shale Pit has lower fracture density than upper section, which means that more fractures can likely be generated through stimulation in rocks similar to the upper section. However the middle section has more systematic fracture sets than the upper section, which implies that when stimulated, more consistent factures can be created. In general, fracture systems provide information on the principal stress directions, which is key in determining the wellbore placement. As the dominant fracture sets observed in the study are perpendicular to bedding and

strike NE, if exploration wells being drilling in the Ardmore and Marietta Basins they can be oriented to not only drill parallel to least principal stress, but also intersect the largest number of fractures.

REFERENCES

Allen, R.W., 2002, Complex Structural Features of Ardmore Basin, Search and Discovery Article #10027.

Ataman, O., 2008, Natural fracture systems in the Woodford Shale, Arbuckle Mountains, Oklahoma: Stillwater, Oklahoma State University, unpublished M.S. thesis.

Badra, H., 2011, Fracture Characterization and Analog Modeling of the Woodford Shale in the Arbuckle Mountains, Oklahoma, USA. Poster presentation. AAPG Annual Convention and Exhibition, Milan, Italy, October 23-26, 2011.

Bellian, J.A., Kerans, C., Jennette, D.C., 2005, Digital Outcrop Models: Applications of Terrestrial Scanning LiDAR Technology in Stratigraphic Modeling: Journal of Sedimentary Research, v. 75, 166-176.

Bernal, A.S., Mayorga, L.C., Prada, A.G., and Slatt, R.M, 2012, Geological Characterization of the Woodford Shale, McAlester Cemetery Quarry, Oklahoma. Shale Shaker, November-December, 202-212.

Blackford, M.A., 2007, Electrostratigraphy, Thickness, and Petrophysical Evaluation of the Woodford Shale, Arkoma Basin, Oklahoma. Oklahoma State University.

Bond, P.I., 2011, Sagebrush Steppe Shrub Height and Canopy Cover Estimation Using LiDAR and Landsat 5 TM Data. Idaho State University.

Brace, W.F., 1961, Dependence of fracture strength of rocks on grain size: Pennsylvania State University Mineral Export Station Bulletin, v. 79, 99-103.

Burton, D., Dunlap, D.B., Wood, L.J., and Flaig, P.P., 2011, Lidar Intensity as a Remote Sensor of Rock Properties: Journal of Sedimentary Research, v. 81, 339-347.

Candela, P. A., 1997, Fractures and Fracturing. *Fractures and Fracturing*. November 11, 2013, from http://www.geol.umd.edu/facilities/lmdr/fractures.html.

Candela, T., Renard, F., Bouchon, M., Brouste, A., Marsan, D., and Schmittbuhl, J., 2009, Characterization of Fault Roughness at Various Scales: Implications of Three-Dimensional High Resolution Topography Measurements. Pure and Applied Geophysics, 166, 1817-1851.

Cardott, B.J. and Lambert, M.W., 1985, Thermal Maturation by Vitrinite Reflectance of Woodford Shale, Anadarko Basin, Oklahoma. AAPG Bulletin, v. 69, no. 11, 1982-1998.

Chipera, S.J. and Bish, D.L., 2013, Fitting Full X-Ray Diffraction Patterns for Quantitative Analysis: A Method for Readily Quantifying Crystalline and Disordered Phases. Scientific Research, *Advances in Materials Physics and Chemistry*, 2013, 3, 47-53.

Comer, J.B. and Hinch, H.H., 1987, Recognizing and Quantifying Expulsion of Oil from the Woodford Formation and Age-Equivalent Rocks in Oklahoma and Arkansas. AAPG Bulletin, v. 71, no.7, 884-858.

Comer, J.B., 2005, Facies distribution and hydrocarbon production potential of Woodford Shale in the southern Midcontinent, in B.J. Cardott, ed., Unconventional energy resources in the southern Midcontinent, 2004 symposium: Oklahoma Geological Survey Circular 110, 51-62.

Corbett, K., Friedman, M., and Spang, J., 1987, Fracture Development and Mechanical Stratigraphy of Austin Chalk, Texas: AAPG Bulletin, v. 71, 17-28.

Ehinger, S.E. 2010, Design, Development, and Application of LiDAR Data Processing Tools. Idaho State University.

Feng, Q.H. and Roeshoff, K. 2004. In-situ mapping and documentation of rock faces using a full-coverage 3D laser scanner technique. *Int. J. Rock Mech. Min. Sci.* 41 (3): 379.

Fritz, R.D., Horn, M.K., and Joshi, S.D., 1991, Geological Aspects of Horizontal Drilling, Tulsa: AAPG, 563

Gross, M., Fischer, M., Engelder, T., and Greenfield, R., 1995, Factors controlling joint spacing in interbedded sedimentary rocks: integrating numerical models with field observations from the Monterey Formation, USA: GSA special publication, v.92, 215-233.

Guo, Y., Zhang, K., and Marfurt, K.J., 2010, Seismic attribute illumination of Woodford shale faults and fractures, Arkoma Basin, OK: 80th Annual International Meeting, SEG, Expanded Abstracts, 1372-1376.

Harris, N.B., Hemmesch, N.T., and Mnich, C.A., 2009, An Integrated Geological and Petrophysical Study of a Shale Gas Play: Woodford Shale, Permian Basin, West Texas. Gulf Coast Association of Geological Societies Transactions, v. 59, 337-346.

Hatcher, D. R., 1995, Structural Geology: Principles, Concepts and Problems: Prentice Halls Inc., 2. Edition, 525.

Hendrick, S.J., 1990, Vitrinite Reflectance and Deep Arbuckle Maturation at Wilburton Field, Latimer County, Oklahoma, *in* Johnson K.S. and B.J. Cardott (eds.) Source Rocks in the Southern Midcontinent, 1990 symposium: Oklahoma Geological Society Circular No. 93, 176-184.

Hennings, P., Olson, J., and Thompson, L., 2000, Combining outcrop data and three-dimensional structural models to characterize fractured reservoirs: An example from Wyoming: AAPG Bulletin-American Association Of Petroleum Geologists, v. 84, no. 6, 830–849.

Hester, T.C., Schmoker, J.W., and Sahl, H.L., 1990, Log-derived regional source-rock characteristics of the Woodford Shale, Anadarko basin, Oklahoma: U.S. Geological Survey Bulletin 1866-D, 38.

Hobbs, C. W., 1967, The Formation of Tension Joints in Sedimentary Rocks: an Explanation, Geological Magazine, v.104, 550-556.

Hunt, J.M., 1995, Petroleum geochemistry and geology: New York, W.H. Freeman and Company, 743.

Inada, R. and Takagi, M., 2010, Method of Landslide Measurement by Ground Based LiDAR: International Archives of the Photogrammetry, Remote Sensing and Spatial Information Science, v. XXXVIII, part 8.

Kemeny, J. and Donovan, J. 2005. Rock mass characterization using LiDAR and automated point cloud processing. *Ground Engineering* 38 (11): 26-29.

Kirkland, D.W., Denison, R.E., Summers, D.M., and Gormly, J.R., 1992, Geology and organic geochemistry of the Woodford Shale in the Criner Hills and western Arbuckle Mountains, in K.S. Johnson and B.J. Cardott (eds.) Source rocks in the southern Midcontinent, 1990 symposium: Oklahoma Geological Survey Circular 93, 38-69.

Laderia, F. L. and Price, N. J., 1981, Relationship between fracture spacing and bed thickness: Journal of Structure Geology, v. 3, n. 2, 183-198.

Lambert, M., 1993, Internal stratigraphy and organic facies of the Devonian-Mississippian Chattanooga (Woodford) Shale in Oklahoma and Kansas: AAGP Bulletin, v. 37, 163-176.

Laubach, S.E., Olson, J.E., and Gross, M.R., 2009, Mechanical and fracture stratigraphy. AAPG Bulletin, 93(11), 1413–1426.

Lewan, M.D., 1983, Effects of thermal maturation on stable organic carbon isotopes as determined by hydrous pyrolysis of Woodford Shale: Geochimica et Cosmochimica Acta, Vol. 47, 1471-1479.

Maher, H.D. Jr., 2007, The nature of cracks. *The nature of cracks (from a geologic perspective)*. November 13, 2013, from http://www.easybib.com/reference/guide/apa/website.

Monte, J.M., 2004, Rock mass characterization using laser scanning and digital imaging data collection techniques. Master Thesis, University of Arizona.

Moore, J., Taylor, A., Johnson, C., Ritts, B.C., and Archer, R., 2012, Facies analysis, reservoir characterization, and LIDAR modeling of an Eocene Lacustrine Delta, Green River formation, Southwest Uinta basin, Utah, in O. W. Baganz, Y. Bartov, K. Bohacs, and D. Nummedal, eds., Lacustrine sandstone reservoirs and hydrocarbon systems: AAPG Memoir 95, 183-208.

Nagihara, S., 2006, Use of ground-based LIDAR in geomorphic and surface stratigraphic studies: Gulf Coast Association of Geological Societies Transactions, v. 56, 659-664.

Narr, W. and Suppe, J., 1991, Joint spacing in sedimentary rocks: Journal of Structural Geology, v. 13, n. 9, 1037-1048.

Nelson, R., 2001**,** Geologic Analysis of Naturally Fractured Reservoirs: Gulf Professional Publishing Company; 2. Edition, 320.

Neman, R.L., 2011, My Favorite Outcrop – The Sylvan Shale, the Hunton Group, and the Woodford Shale: Shale Shaker, May-June, 343-349.

Pollard, D.D. and Aydin, A., 1988, Progress in understanding jointing over the past century. Geological Society of America Bulletin, v. 100, 1181-1204.

Portas, R.M. and Slatt, R., 2010, Characterization and Origin of Fracture Patterns in a Woodford Shale Quarry in Southeastern Oklahoma for Application to Exploration and Development. Poster presentation. AAPG Annual Convention and Exhibition, Louisiana, LA. 11-14 Apr. 2010.

Price, N. J., 1966, Fault and Joint development in brittle and semi-brittle rock: Pergammon Press, London, 176.

Puckette, J., Boardman, D., and Watney, L., 2013, "Woodford Shale: Correlating Rock Properties in Outcrop and Core to Wireline Log Characteristics." PowerPoint presentation. Double Tree by Hilton, Wichita, KS. 14 Oct 2013.

Romero, A.M. and Philp, R.P., 2012, Organic geochemistry of the Woodford Shale, southeastern Oklahoma: How variable can shales be?. AAPG Bulletin, v. 96, no.3, 493-517.

Rotevatn, A., Buckley, S.J., Howell, J.A., and Fossen, H., 2009, Overlapping faults and their effect on fluid flow in different reservoir types: A LIDAR-based outcrop modeling and flow simulation study: AAPG Bulletin, v. 93, 407-427.

Scintag, Inc., 1999, Chapter 7: Basics of X-ray Diffraction. Retrieved November 20, 2012, from http://epswww.unm.edu/xrd/xrdbasics.pdf.

Sturzenegger, M., Yan, M., Stead, D. and Elmo, D., 2007, Application and limitations of ground-based laser scanning in rock slope characterization. In proceedings: 1st Canada-US Rock Mechanics Symposium, 27-31 May 2007, Vancouver.

Sullivan, K.L., 1985, Organic Facies Variation of the Woodford Shale in Western Oklahoma. Shale Shaker Digest XI, v. 33-35, 185-198.

Underwood, C. A., Cooke, M. L., Simo, J. A., and Muldoon, M. A., 2003, Stratigraphic controls fracture patterns in Silurian dolomite, northeastern Wisconsin: AAPG Bulletin, v. 87, no. 1, 121-142.

Varacchi, B.H., 2011, Rock Physics and Mechanical Stratigraphy of the Woodford Shale, Anadarko Basin, Oklahoma. Oklahoma State University.

Walker, W.M., 2006, Structural Analysis of the Criner Hills, South-Central Oklahoma, Baylor University, M.S. thesis.

Wozencraft, J. and Millar, D., 2005, Airborne Lidar and Integrated Technologies for Coastal Mapping and Nautical Charting *in* Marine Technology Journal, Vol 39, Number 3, Fall 2005.

APPENDICES

Appendix A

Field Steps

Riegl USA

Operation Check List for VZ 400 Pre-Scanning set up

Provided By: The Core Facility for Laser-Based Three-Dimensional Scanning

1. Scanner Set Up: Mount scanner on tripod.

2. Power Connection: Connect power cable to the scanner Power 1 outlet and separately connect the cable to the power source.

3. Connect the two ends of the power cables. This will start the scanner automatically. If it doesn't start automatically, hold the ON/OFF button for three seconds.

4. Camera Set Up: Plug the USB cable into the camera and then to the scanner.

5. Place the camera on top of the scanner (lens of camera facing front mirror of the scanner). Fasten camera mount to scanner by securing the side screws.

6. Turn the camera ON.

7. RiSCAN PRO Set Up: Open RiSCAN PRO and create a new project.

8. In the Calibrations folder right click on Reflector folder and select New Reflector. Enter reflector name, scale and size. (only for cylindrical reflectors).

9. Go to Tool>Options>Units and select proper units.

10. In the Project Manager tab, right click on the project name and select Attributes. In the Instrument tab under scanner IP enter instrument serial number. Make sure Nikon D700 camera model is selected.

11. Communication: Connect the cross over network cable to the laptop (small green cable with red tape).

12. Plug Communication TCP/IP (green) cable to the scanner.

13. On the scanner's screen select Settings/Systems/LAN&WLAN. Set to LAN0 (100 Mbit) and Config to DHCP_SERVER. Click Home.

14. Back on the computer, click on Start and select Control Panel. Open the Network and Sharing Center and click on Manage Network Connections. Right click on Local Area Connection and select Properties. Select Internet Protocol Version 4 (TCP/IP V4) and click on Properties.

15. Check Obtain and IP Address Automatically.

16. In RiSCAN PRO Click on the scanner connection status icon (Network Connection State of Scanner). The following message should appear in the message list if the scanner is communicating: Scanner "//s9997464.20002" detected.

17. When the computer is communicating to the scanner, the message 'scanner S9997397 2000 Detected' will appear in the message list window in RISCAN PRO in blue letters.

18. Go to Tool>Camera Configuration (V Line) and select proper exposure settings. If Automatic mode is selected to get the best exposure mode, change back to Manual mode before closing window.

19. Environmental Conditions: Right click over project name (first line in blue letters on the project manager tab) and select Attributes>Scaling Correction enter Temperature (Celsius), Barometric Pressure (mb), Dew Point Temperature (Celsius), Relative Moisture Percent, Mositure Pressure (mb). Click on Atmospheric Settings to send information to the scanner.

20. Validation: Right click on SCANS folder and select New Scan Position. Rename this scan position to VALIDATION. Right click on VALIDATION and select New Single Scan. Click on Overview. On the scanner configuration window, check Download data to project and Image Acquisition. Select from the list the corresponding Camera Model and Lens. Make sure Online View is 2D and select Scan Mode High Speed. Click Ok.

21. Once scan and acquisition of images is finished. Find three (3) targets and fine scan them.

22. Image Adjustment: select images that contain fine scanned targets. Hold Ctrl+2 to display SOCS on each picture. If all targets have the same offset, eyeball the center of the target, left click and right click it. Select add point to TPL and click OK for each picture. (need to make at least 3 links).

23. Right click on each picture and select Autolinker. Enter 100 and click OK. Targets linked change colors.

24. Go to Calibrations>Mounting and select the loaded mounting and click on Readjustment of Camera Mounting Tab. Click on Start Readjustment. Solution should be less than a pixel.

25. If everything is running fine, you are ready to move to the first position.

26. Control (optional): to enter control (GPS coordinates), right click on TPL GLCS and select import. Browse for a CSU or text file that contains GPS coordinates for the control in Cartesian Coordinates (XYZ) and click Open.

27. If there is a header, check skip # of lines, and enter how many lines to remove. If columns are not defined, select auto detect to separate columns.

28. Drag and drop on the appropriate header to each column in the following order

Name

X: Easting

Y: Northing

Z: Elevation

Click Ok and all points are copied in the TPL GLCS list

29. Open TPL GLCS and hold Ctrl A to select all the points. Right click on any of the highlighted points and select copy tie point to PRCS. Click OK to save coordinates names and OK for the truncation. All control should be in TPL PROCS now.

30. Open TPL PRCS and select control points with height offset. Right click on such highlighted points and select set reflector height and enter height of the center of the target to the control point elevation. If control point is below the target, enter a positive offset and vice versa.

Operation Check List

1. In RiSCAN PRO, close all previous scanned windows to preserve RAM. Right click on SCANS and select New Scan Position. Right click on ScanPos## and select New Single Scan.

2. In the scanner configuration window, click Panorama to reset angles to a 360 scan and Survey Grade resolution. Make sure Online View is 2D and select proper Scan Mode (High Speed-Indoors/Outdoors or Long Range – Outdoors)

3. Check Download data to project and Image Acquisition. Select from the list the corresponding Camera Model and Lens. Click Ok.

4. Once scan is downloaded, find a target. Right Click on the target (red or white spot), select Create tiepoint here. Naming targets has no influence in the registration process.

5. Once you have found and marked all targets, wait until the scanner has completed the scan and images collection.

6. Double click on TPL SOCS and select all targets. Click on Fine Scan Selected Tiepoints icon. As the scanner scans the targets, make sure all targets have a square or circular white or red shape. If any targets has no particular shape, check on the 3D scan.

7. Once the scanner has completed the fine scan of all targets, register the scan position previous positions. For first scan only: right click over scan position name and click on Registered. Open TPL SOCS and Click on Find Corresponding Points icon. Make sure Project Coordinate and any other relatively close positions are checked. Adjust minimum number of tiepoints depending on how many targets it can match to control and/or other scan positions. Click on Start.

8. Usually the first solution is the best. If the standard deviation is within the control accuracy or scanner relative accuracy (if no control points have been entered), then click OK. If it is not, click on next solution to get other registration solutions. Click Ok. The best solution is a combination of the maximum number of corresponding points with a low standard deviation of residues.

9. If necessary, make a visual QA/QC of the data by dragging 2 or more scans of different positions in 3D and cutting cross sections of data to compare that common surfaces are matching. Based on this scan view, identify the next position.

10 If registration is correct, move to the next position.

To undo registration:

1. Open TPL PRCS and delete all tie points
2. Open POP, right click on matrix and select default

On each scan position:

3. Right click over position name and uncheck register.
4. Open SOP and right click over the matrix. Select set to default
5. Open Tiepoint scans list and go over list to remove unwanted tiepoint finescans
6. Open TPL SOCS to remove from the list the targets that have no fine scan.
7. Record the corresponding type of target to the finescan name of the target (only when using multiple types of targets)
8. Delete all targets and hold Ctrl R to refresh targets
9. Enter appropriate target types by highlighting selected targets and right click over them. Choose set reflector type.
10. This will end the unregistration process, save project and empty trash can

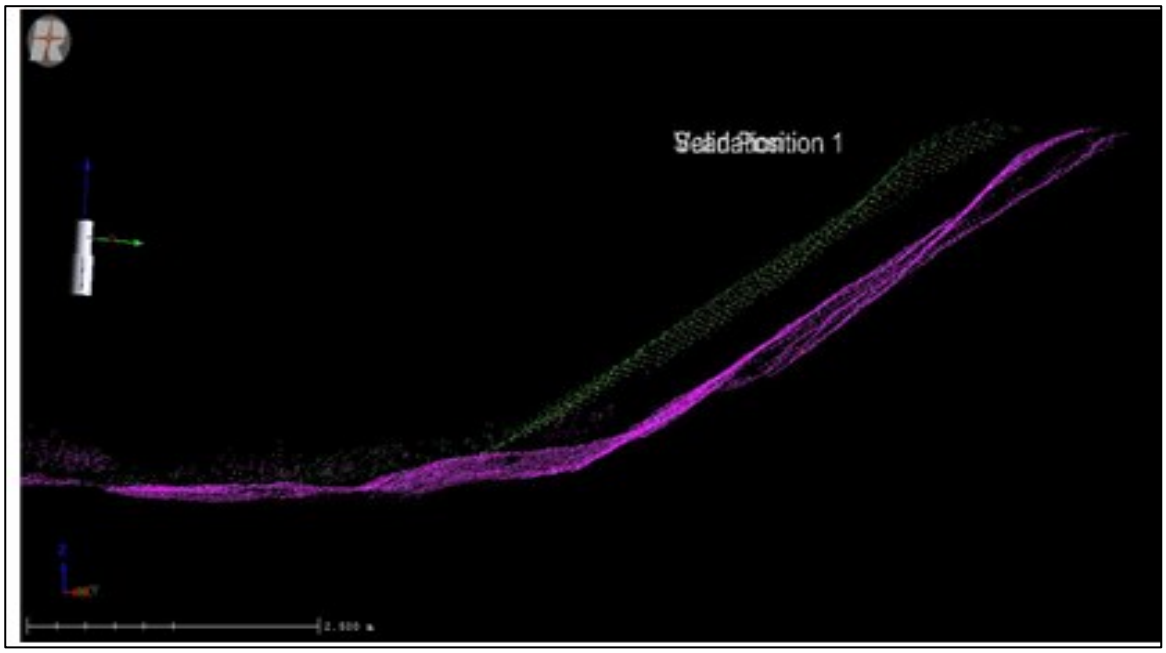

Figure 22 - Screen captured image in RiSCAN PRO prior to a multi-station adjustment. Notice the vertical separation between different scan positions in for the same surface.

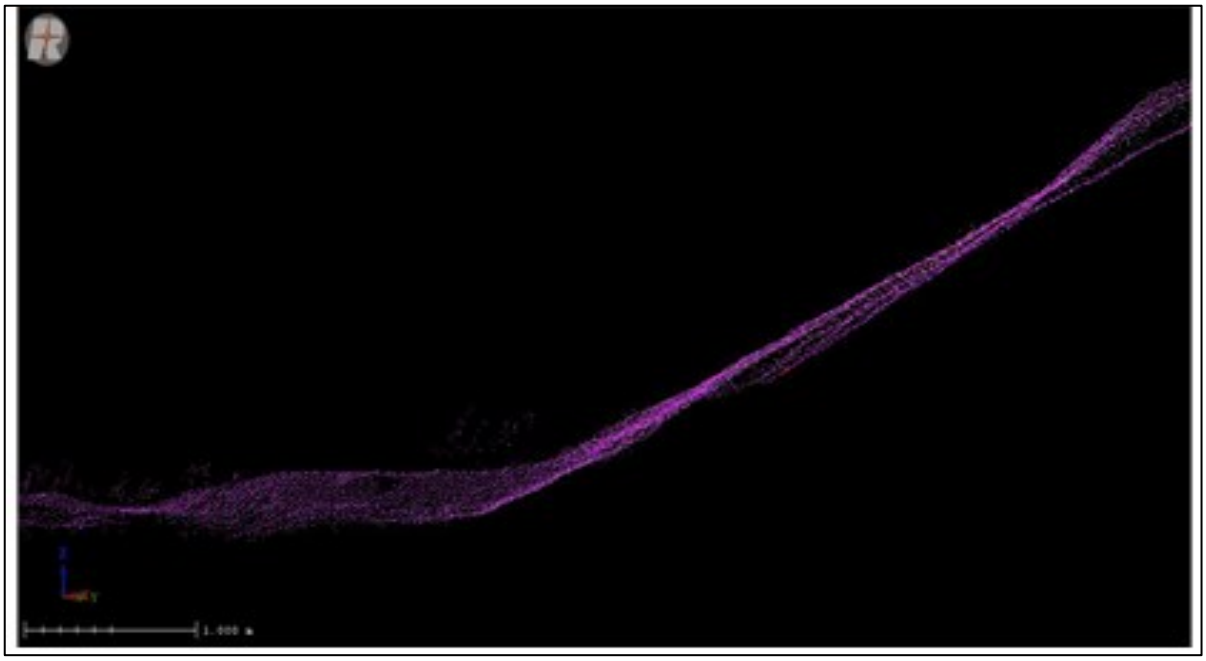

Figure 23 - Screen captured image in RiSCAN PRO after the multi-station adjustment. The point cloud is now cohesive and vertical separation has been eliminated.

Coloring Scans

In project manager select a scan position then highlight all the scan images, right click and select undistort, this is to texture the mesh in RiSCAN PRO. Then select a scan from the same scan position and right click on the scan; selecting color from images. Under images available changing the selection from distorted images to undistorted images will allow undistorted images to be selected. Once the scan selected is matched with the undistorted scan images clicking ok, the software will apply the images to the scan (Figure 24).

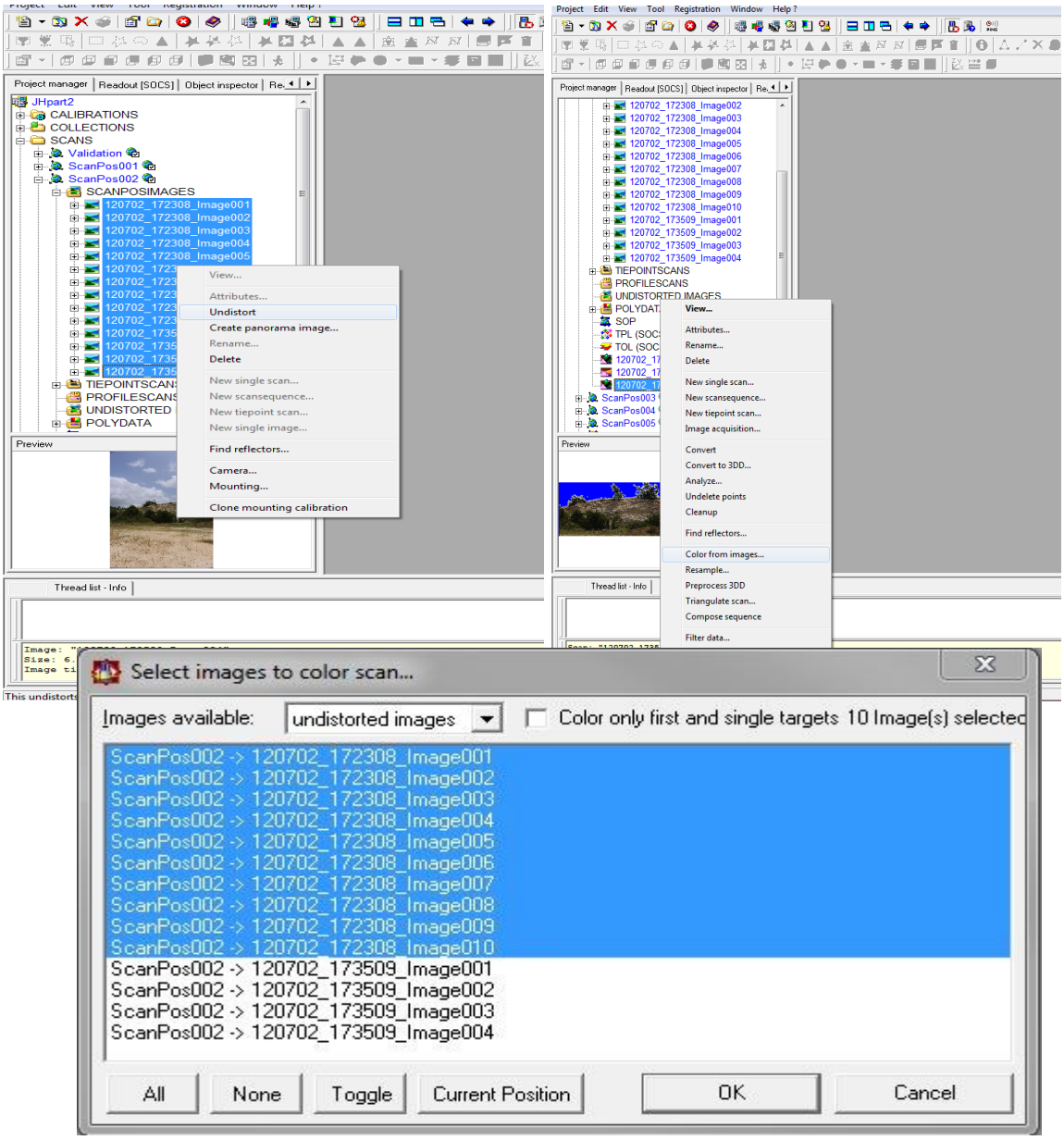

Figure 24 – Process of coloring images in RiSCAN PRO.

Converting Scans

An inability to view a scan to its entirety in 3D is an error that can occur when trying to analyze large high resolution scans (Figure 25). When this happens converting the scans will allow the scan to be seen in 3D. When this issue is noticed, right clicking on the SCANS folder (Figure 26) and selecting convert all scans will solve the problem. This process will convert all of the scans taken, if the scans have been colored prior to this they will have to be recolored after (Figure 27).

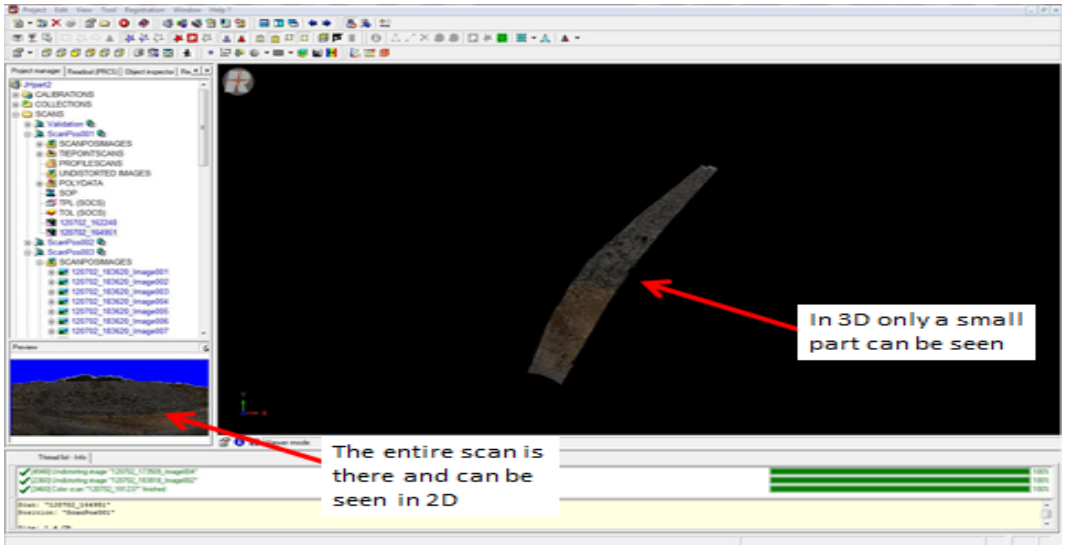

Figure 25 – RiSCAN PRO image in 3D view of a high resolution scan compared to 2D view in bottom left corner.

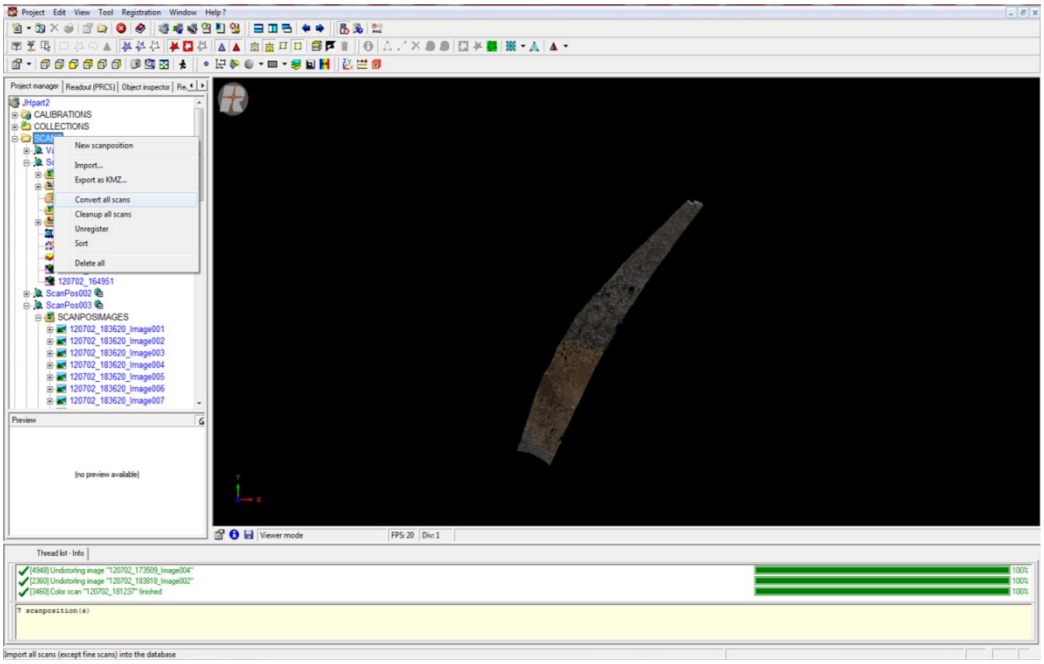

Figure 26 – RiSCAN PRO image in 3D view of a high resolution scan before converting all scans.

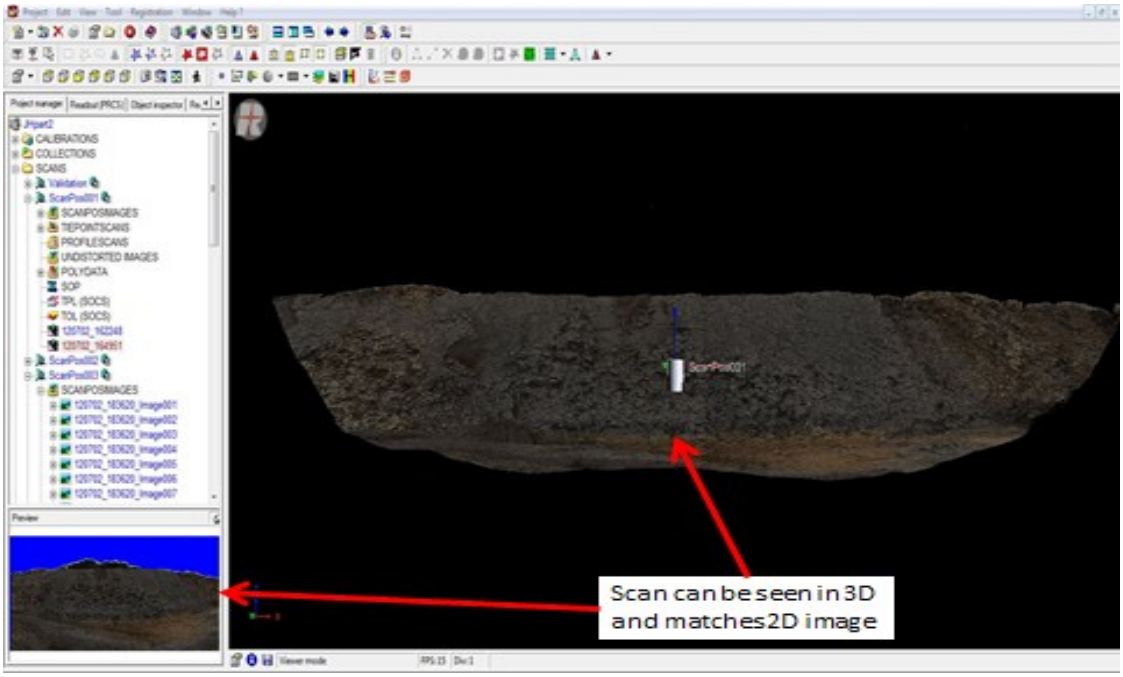

Figure 27 – RiSCAN PRO image in 3D view after converting all scans.

Exporting Scans as ASCII files

After opening a project and viewing the data in 3D hit the space bar and select the data points that are to be exported with the left mouse button. Once done right clicking on the mouse, the data selected will turn red. Then select *Create New Polydata Object*, which is circled and arrowed in the image. A window will show up after clicking this button asking where to place the data. Clicking *No* will store the polydata in the objects file (Figure 28).

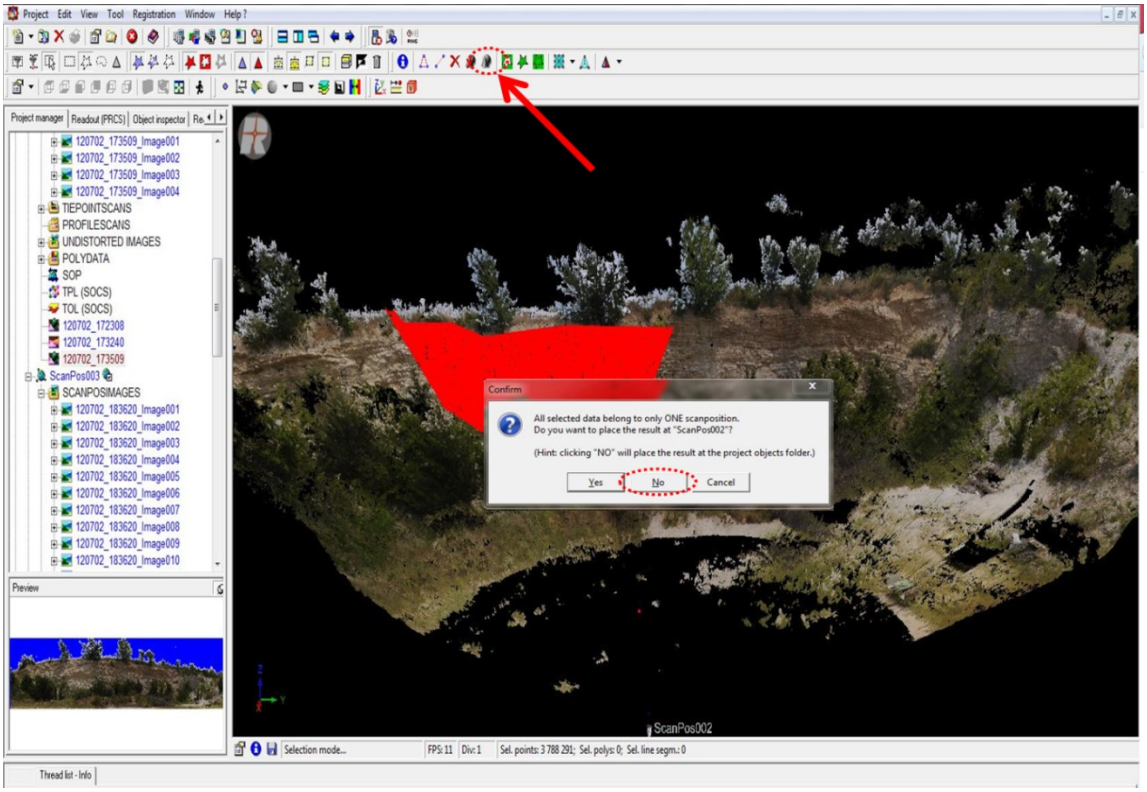

Figure 28 – RiSCAN PRO image in 3D view depicting how to create polydata for export.

Under the objects file in project manager the polydata should be seen called *Polydata001,* right click on the file and select *export*. A window will appear and ask where you would like to store the data, the file can be renamed here, and finally going down to the save as type drop down menu and selecting the data as ASCII which is a XYZ format (Figure 29).

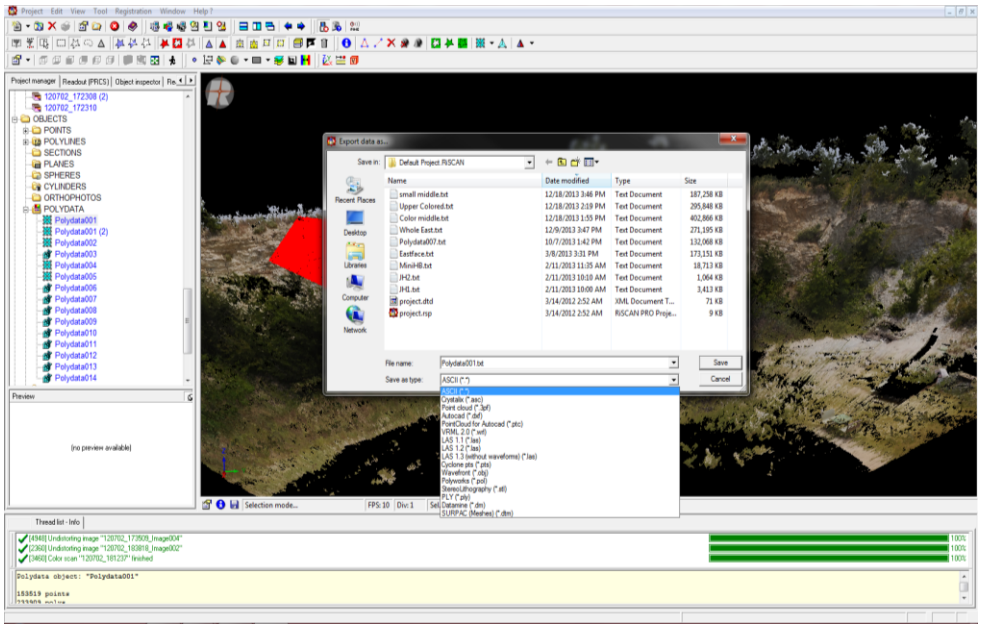

Figure 29 – RiSCAN PRO image displaying how to save polydata prior to being exported.

Another window will pop up; here in general settings make sure PROCS is set. Global coordinates when imported were converted to the PROCS. In Export Format you have XYZ checked and if you want to export the point cloud with color select RGB as well. Push Ok and the file will be created (Figure 30).

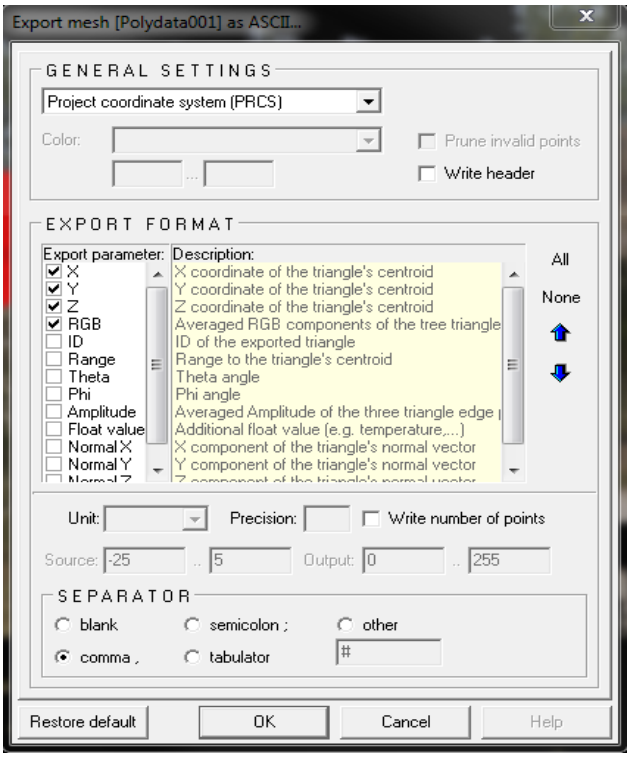

Figure 30 – General settings used to control the parameters of the exported data in RiSCAN PRO.

Appendix B

Importing ASCII file into Split-Fx

After opeing Split-Fx selecting the open button will allow for the RiSCAN PRO ASCII text file to be selected. Once selected a file format window will appear (Figure 31).

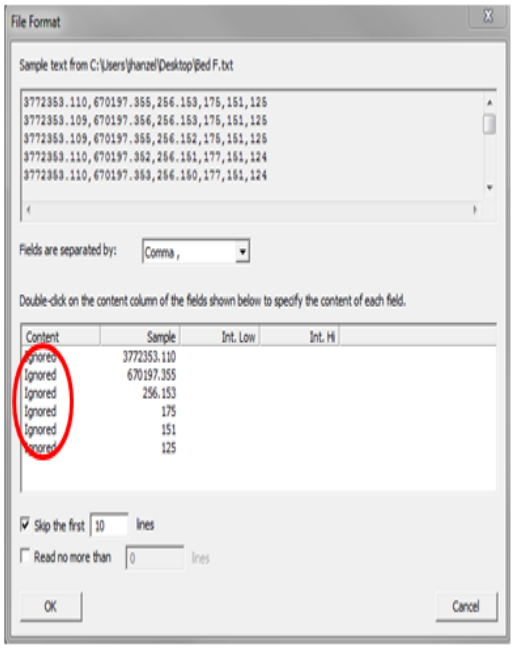

Figure 31 – Image of the importing file format window in Split-Fx.

Under Content select each ignored label and change them to X,Y,Z and R,G,B (note if a non-colored data set is being imported only X,Y,Z is needed). It is a default setting to skip the first 10 lines. Select Ok (Figure 32).

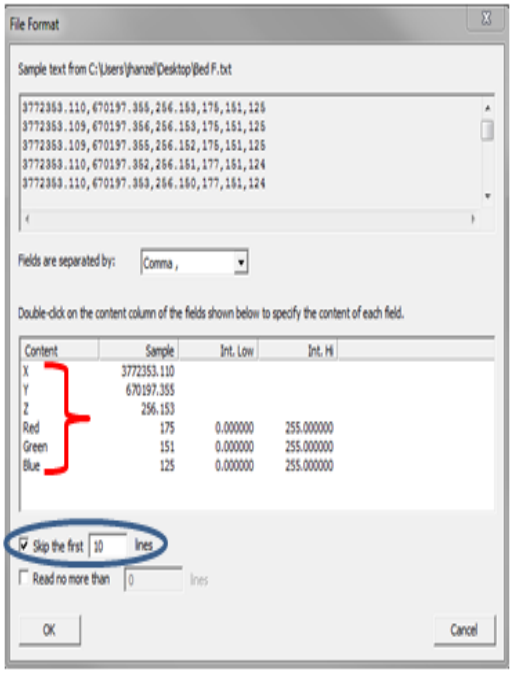

Figure 32 – Image of the importing file format window in Split-Fx after being modified to import XYZ RGB data.

The data will load and a point cloud image will appear. If the points are not, shown depress the button circled in red (Figure 33).

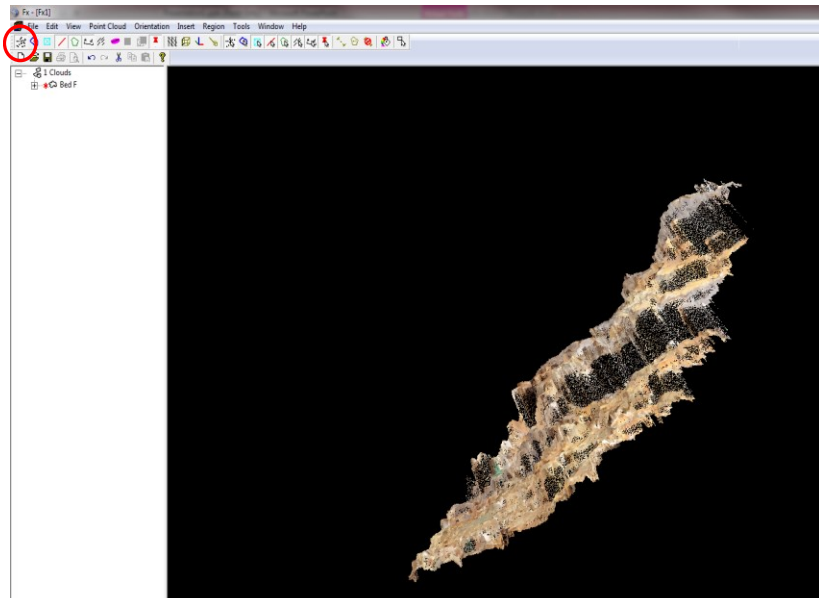

Figure 33 – Colored point cloud image after being imported into Split-Fx.

To create a mesh select Point Cloud, then Create Mesh… once selected the following mesh parameters will appear (Figure 34). It is common to accept the default settings and based on the mesh adjust if necessary (Figure 35).

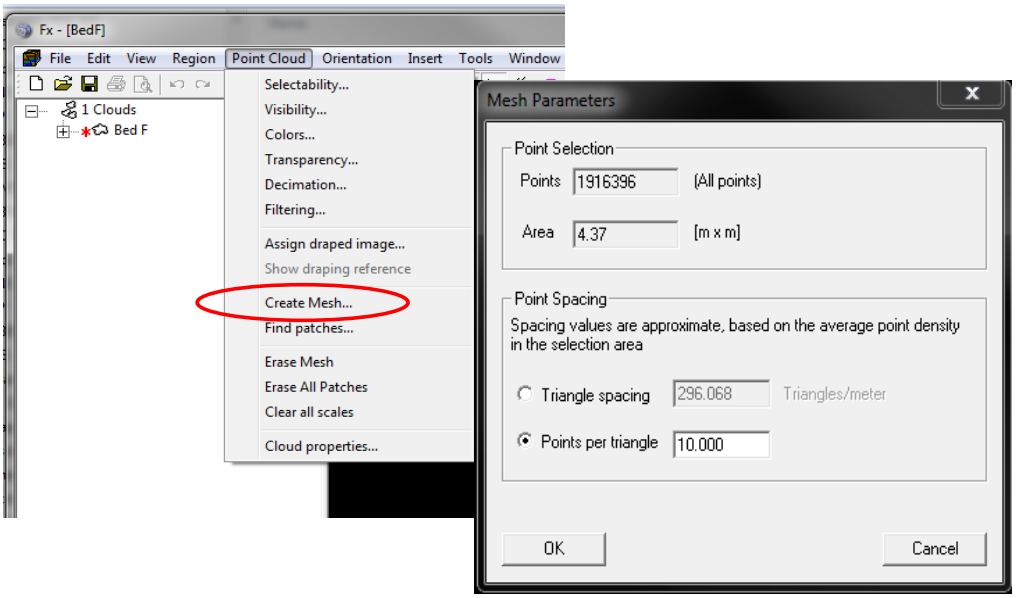

Figure 34 – Creating a mesh parameters window.

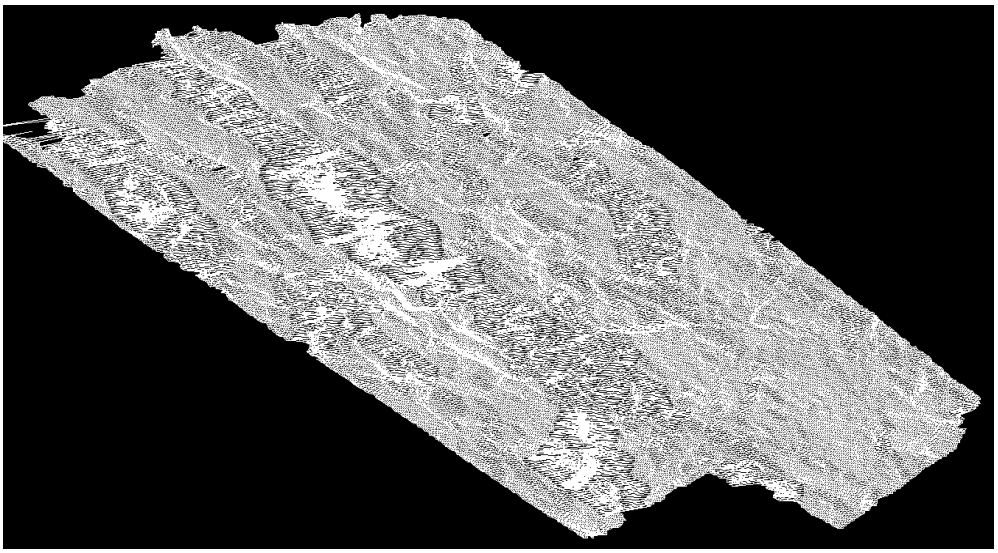

Figure 35 – Generated mesh in Split-FX from the middle section of the Woodford Shale.

After the mesh is created, patch parameters can be set to have automated planes created on the mesh. To create patches select Point Cloud, then Find patches… once selected the following mesh parameters will appear (Figure 36). It is common to accept the default settings and based on the results changes can be made to the filters, size or angles. For large point clouds this process can take several minutes.

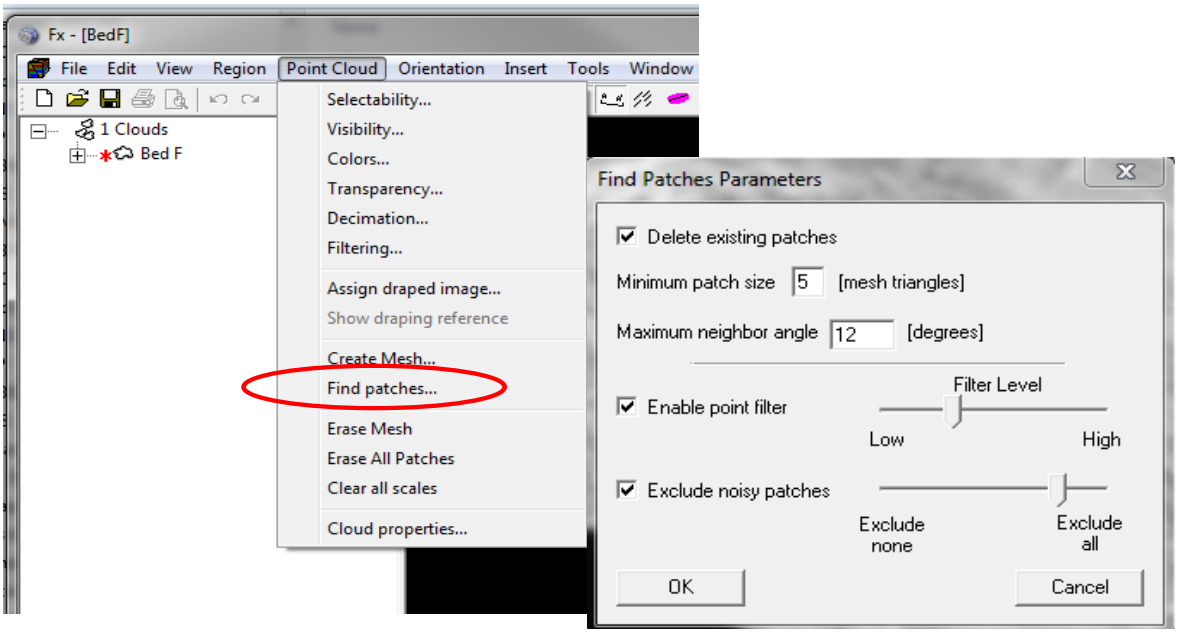

Figure 36 – Finding patch parameters window.

Once patches appear on the mesh, a stereonet can be viewed to double check patch orientations. This is done by selecting region and clicking Stereonet View. A lower hemisphere stereonet plotting poles will appear (Figure 37).

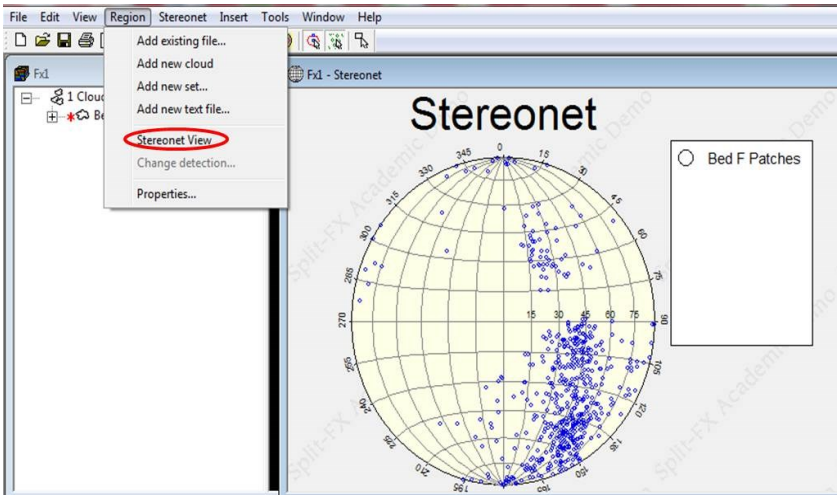

Figure 37 – Visualization of patches in a lower hemisphere stereonet view.

More patches can be added or patches can be modified. Traces are commonly used for hand pick data because when traces are drawn a triangle notes the pole instead of a circle. This makes it easier for the user to track their works. Patches or traces can be put on the mesh manually by selecting insert and either patch or trace. Once selected an insert trace or patch window will appear select ok (Figure 38).

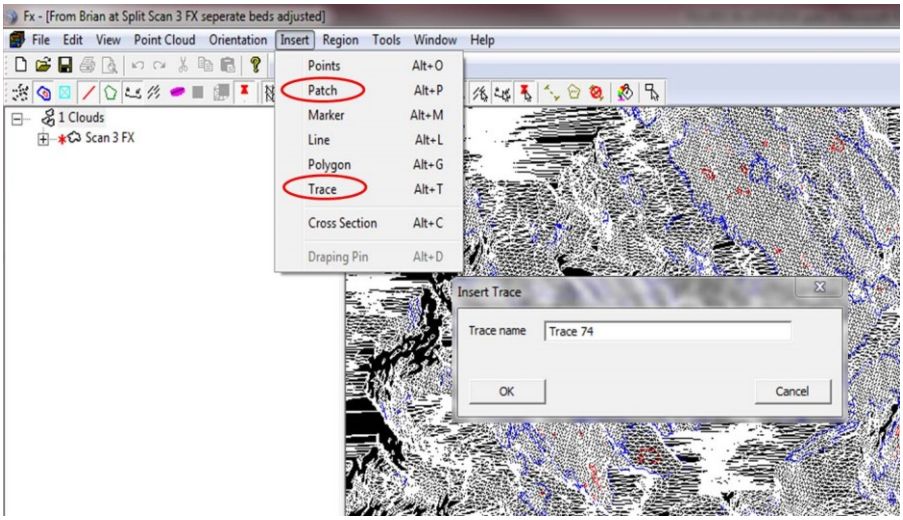

Figure 38 – Inserting a patch or trace in Split-Fx.

Clicking at least 3 points to create a polygon on the mesh will insert a trace or patch. Traces when draw will look like this, Figure 39, on the stereonet.

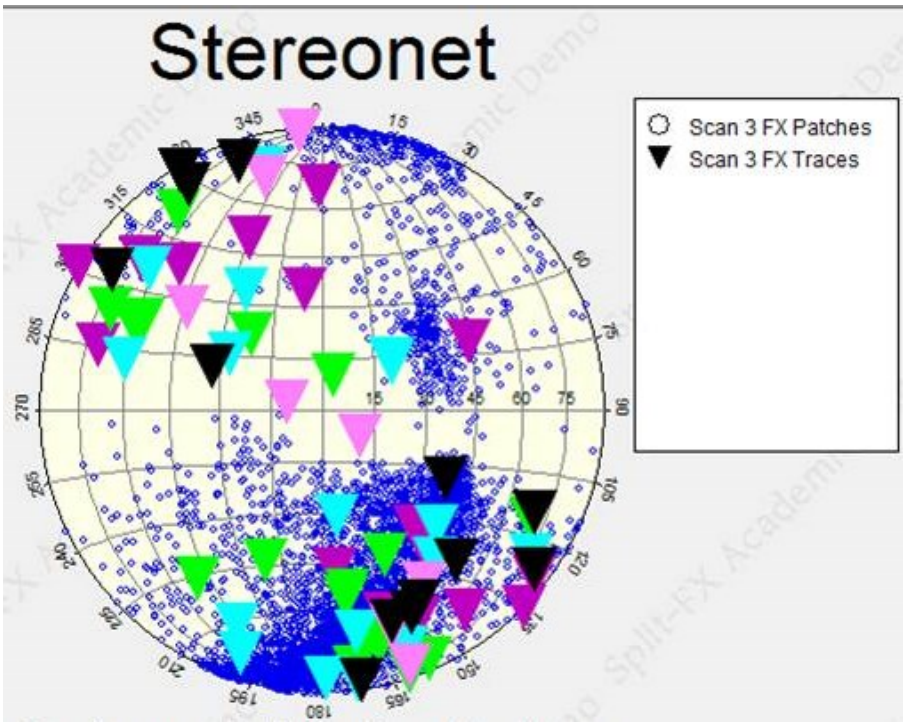

Figure 39 – Visualization of both patches and traces on a stereonet in Split-Fx.

Exporting from Split-Fx

To export stereonet data from Split-Fx go to region, Stereonet View. Highlight the stereonet or just part of the stereonet you would like to export (Figure 40).

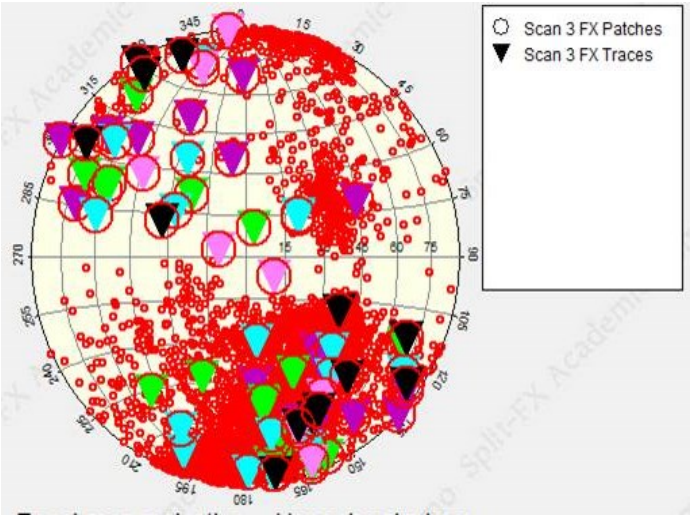

Figure 40 – Highlighted stereonet of both patches and traces in Split-Fx for exporting.

Once highlighted return to the point cloud window, Select file, Export Cloud Data (Figure 41).

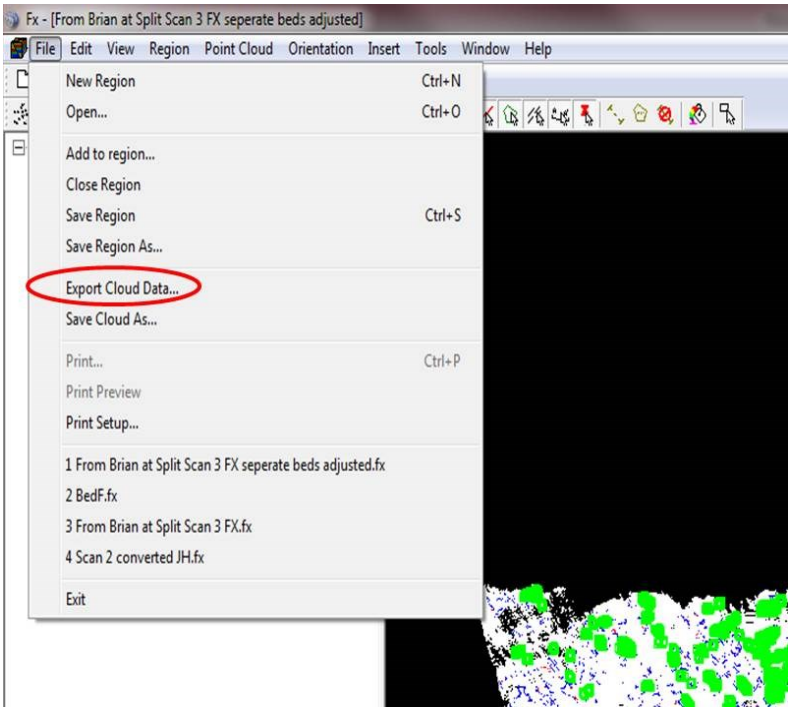

Figure 41 – Exporting cloud data from Split-Fx.

Once selected format output will appear. Depending on what is desired to be exported select patches or Trace Planes. Formatted Normal should be selected as well as Output Selection (Figure 42). Once done selecting Ok will bring up a separate window with all the strike and dip measurements. This can be saved as a text file and imported to other software if need (Figure 43).

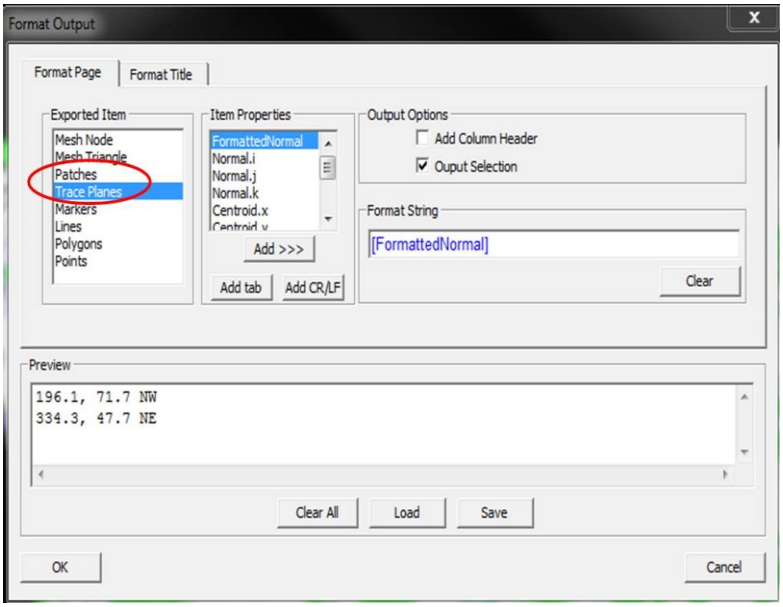

Figure 42 – Export output screen in Split-Fx.

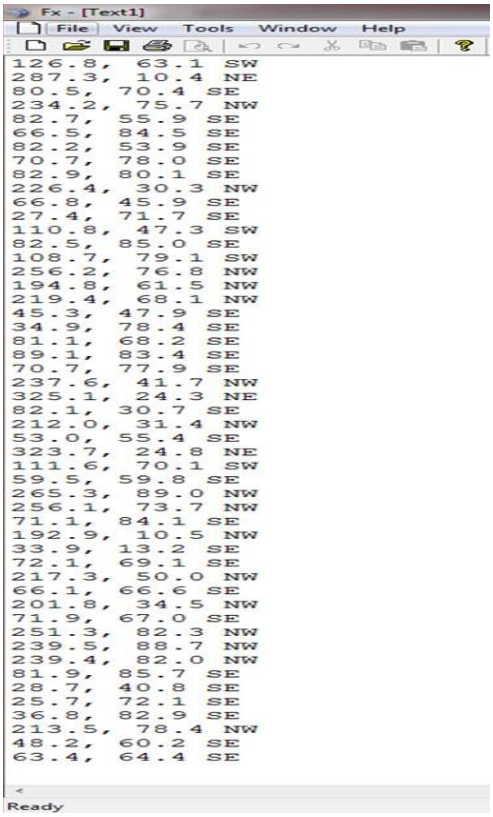

Figure 43 – Screen capture of strike and dip measurements exported from Split-Fx.

Appendix C

XRD and Thin Sections

Thin Section and XRD Comparison

Thin sections were used to better understand XRD derived composition (e.g., Figures 44 – 53).

Figure 44 - Thin section made from the middle section of the Woodford Shale under 10x magnification. Gypsum was found abundantly filling the fractures in thin section view.

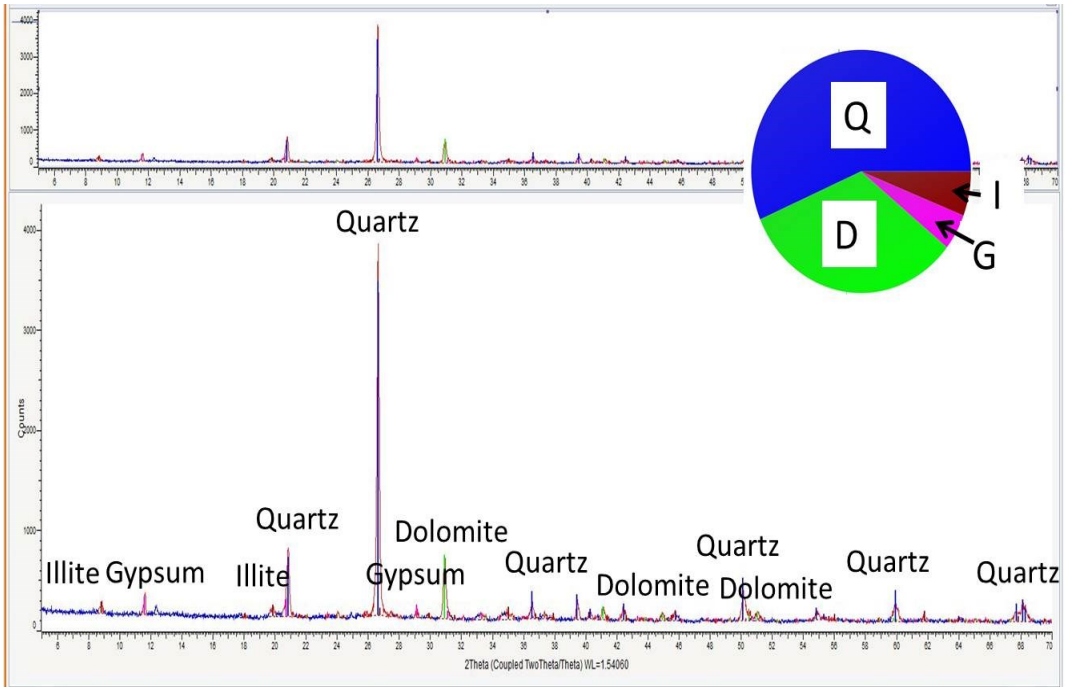

Figure 45 - XRD scan from middle section of the Woodford Shale showing identified gypsum.

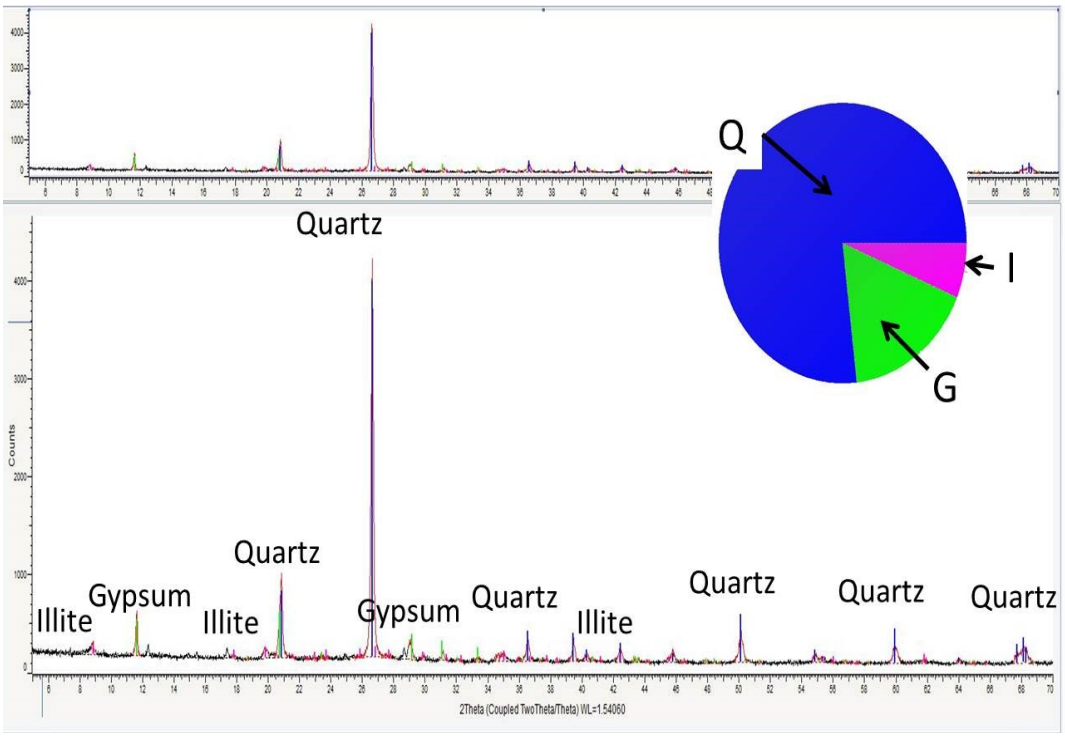

Figure 46 - XRD scan from middle section of the Woodford Shale showing identified gypsum.

Typical XRD Scan for Upper and Middle Sections

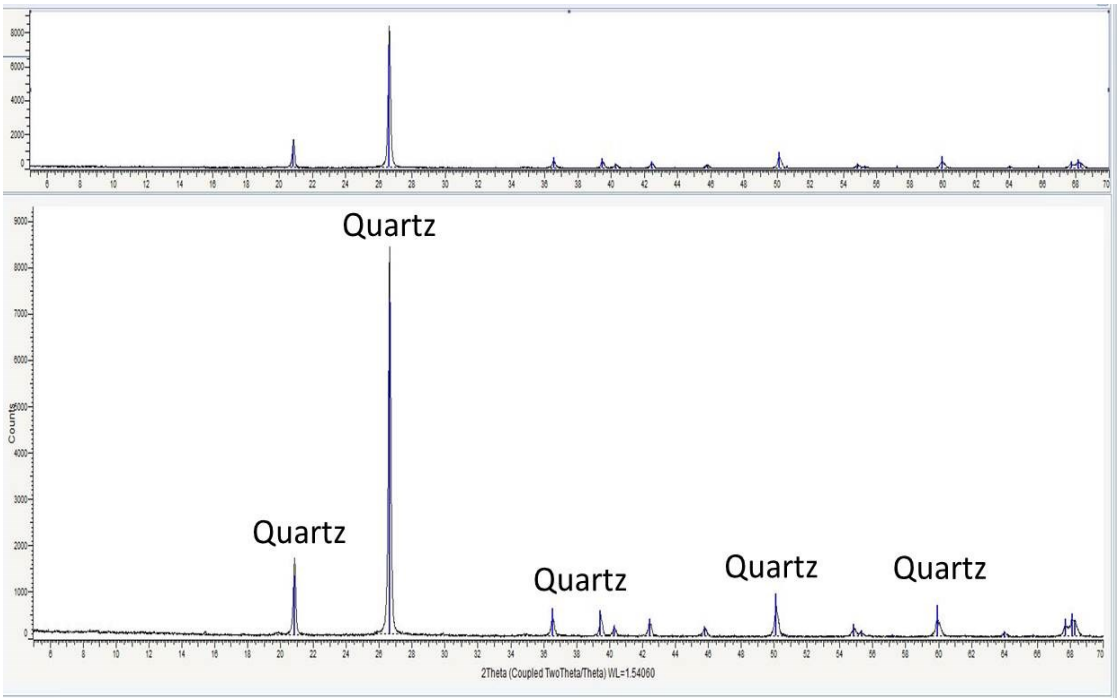

Figure 47 – Representative sample of a chert bed from the upper section of the Woodford Shale.

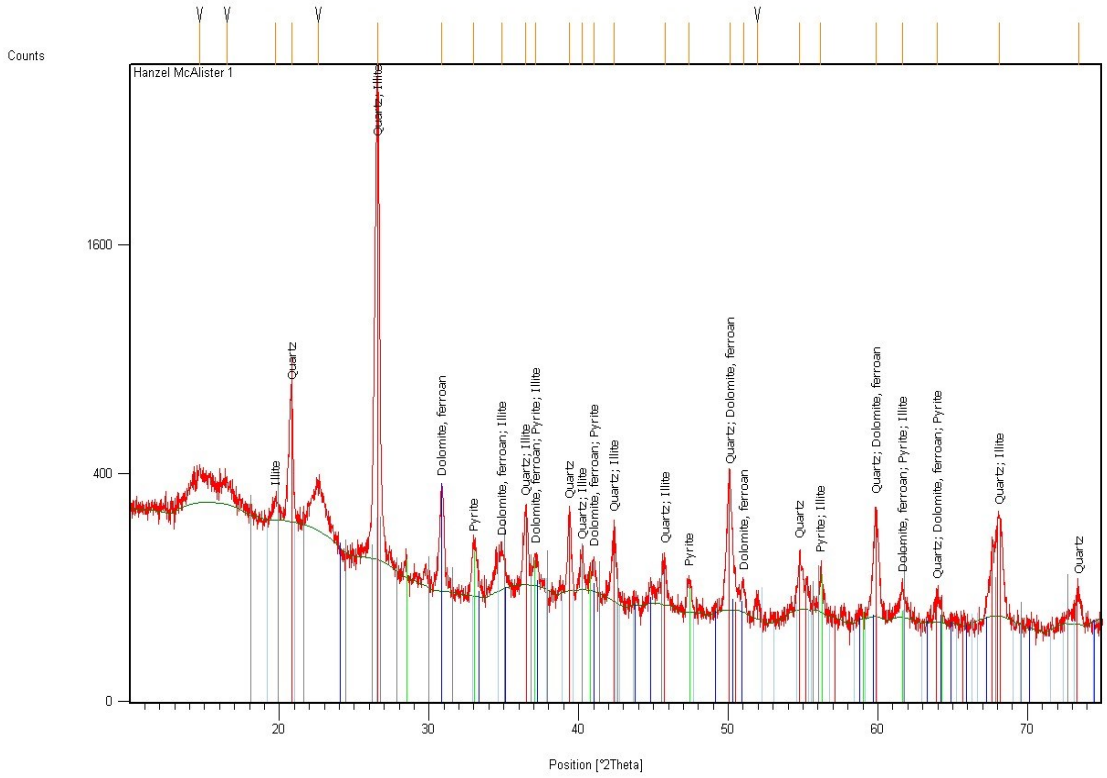

Figure 48 – Representative sample from the middle section of the Woodford Shale showing the presence of clay (illite), carbonate (dolomite), quartz and pyrite.

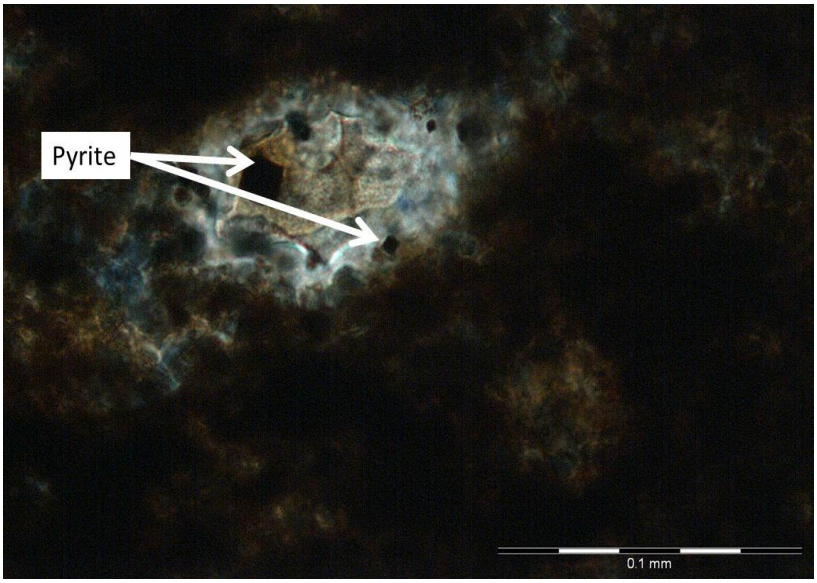

Figure 49 - Sample from the middle section of the Woodford Shale under 20x magnification confirming the presence of pyrite.

Thin Section Images

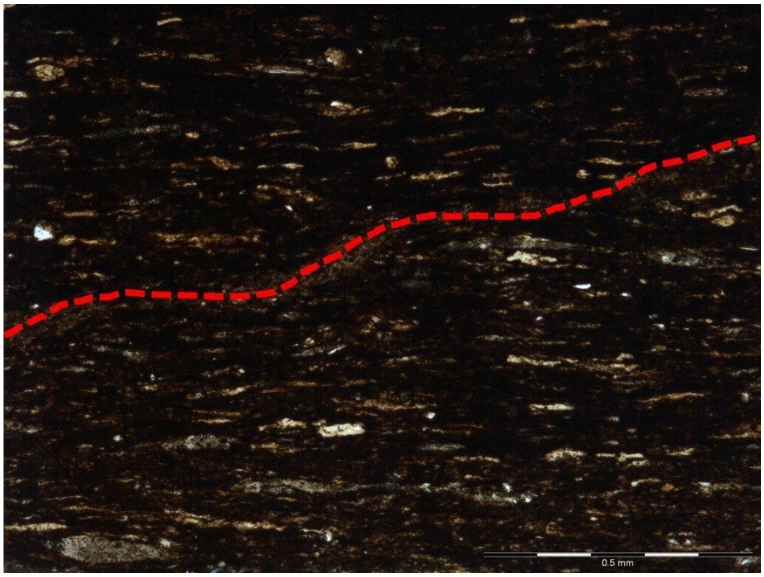

Figure 50 - 5x magnification of a sample in the middle section of the Woodford Shale showing a non-systematic fracture in an organic-rich laminae.

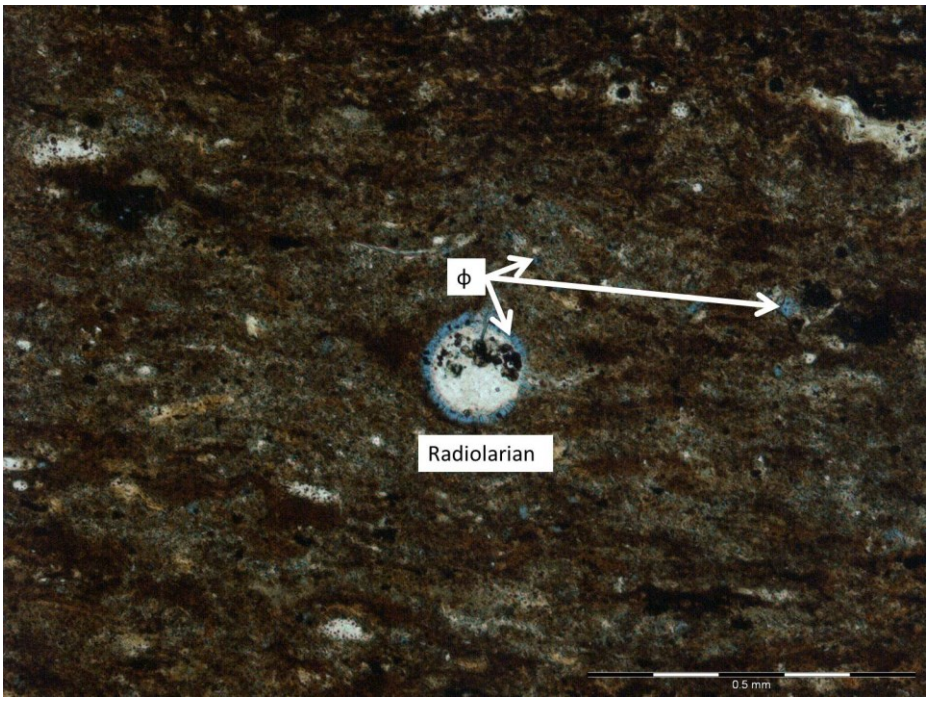

Figure 51 - Sample from the upper section of the Woodford Shale under 5x magnification depicting a radiolarian with micro porosity.

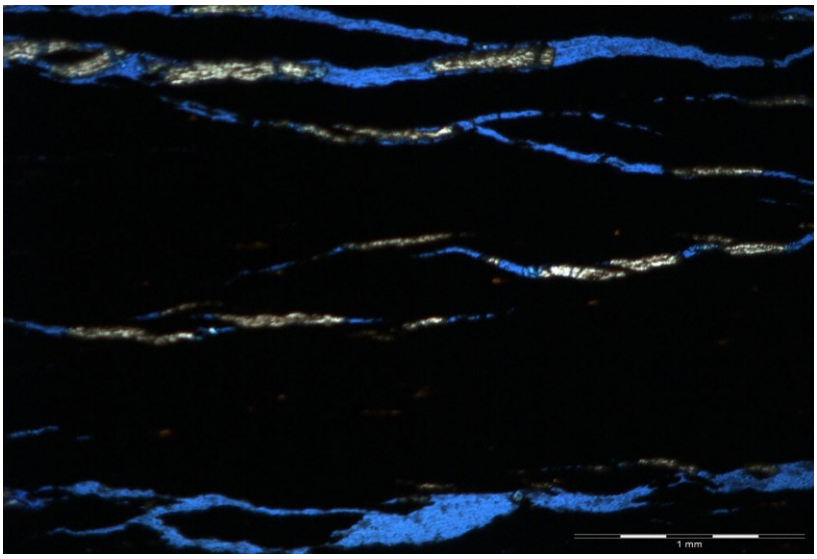

Figure 52 - Micro-fractures parallel to bedding observed in the middle section of the Woodford Shale.

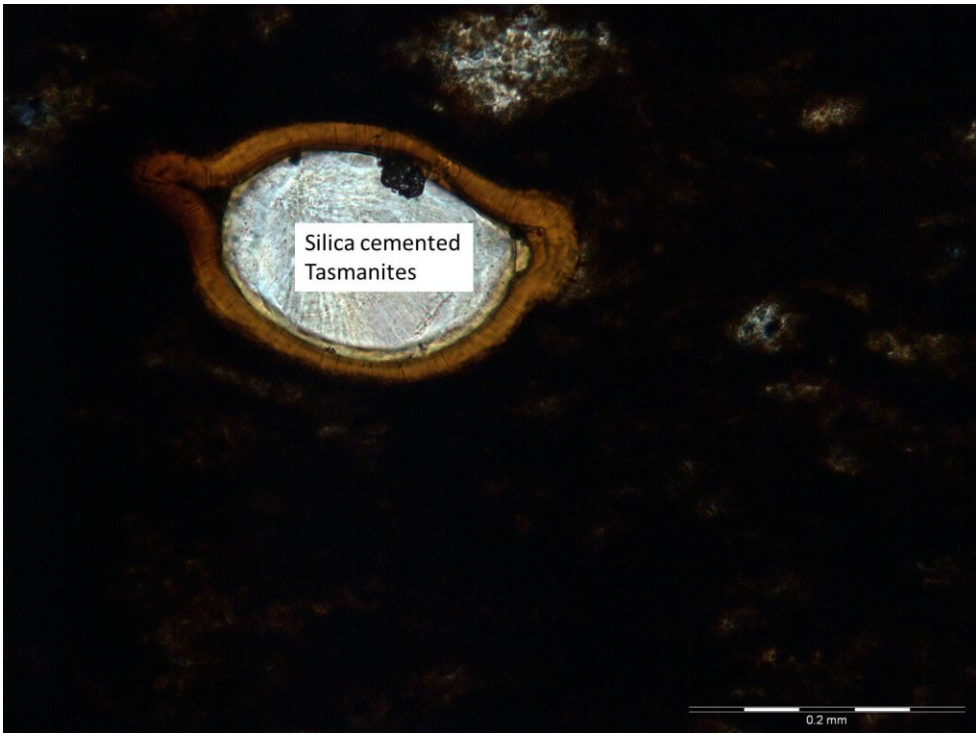

Figure 53 - A preserved prasinophyte alga, *Tasmanite* in 10x magnification, from the middle section of the Woodford Shale.

VITA

Jason Elliott Hanzel

Candidate for the Degree of

Master of Science

Thesis: LIDAR-BASED FRACTURE CHARACTERIZATION: AN OUTCROP-SCALE STUDY OF THE WOODFORD SHALE, MCALISTER SHALE PIT, OKLAHOMA

Major Field: Geology

Biographical:

Education: Completed the requirements for the Master of Science in Geology at Oklahoma State University, Stillwater, Oklahoma in July, 2014. Completed the requirements for the Bachelor of Science degree in Geology at Oklahoma State University, Stillwater, Oklahoma in May, 2012.

Experience: Geology internships at EOG Resources (2010), and Concho Resources (2013). Employed as introductory geology laboratory teaching assistant for two years and research assistant for one year by Oklahoma State University.

Professional Memberships: American Association of Petroleum Geologists, Geological Society of America, Society of Exploration Geophysicists, and the Tulsa Geological Society